FINAL TECHNICAL REPORT
TWO-COLOR HOLOGRAPHY CONCEPT (T-CHI)

Prepared by

C. S. Vikram*, H. J. Caulfield* and G. L. Workman+

The University of Alabama in Huntsville
Huntsville, Alabama 35899
*Center for Applied Optics
+Johnson Research Center

J. D. Trolinger and C. P. Wood
Metrolaser
18006 Skypark Circle, Suite 108
Irvine, California 92714

and

R. L. Clark, A. D. Kathman and R. M. Ruggiero
Teledyne Brown Engineering
300 Sparkman Drive, Mail Stop 19
Huntsville, Alabama 35807

Submitted to

National Aeronautics and Space Administration
George C. Marshall Space Flight Center
Marshall Space Flight Center, Alabama 35812

Contract No. NAS8-38078

April 1990

(NASA-CR-184240) TWO-COLOR HOLOGRAPHY CONCEPT (T-CHI) Final Report (NASA) 65 p
CSCL 14E

N92-10183

Unclas
G3/35 0046415

PRECEDING PAGE BLANK NOT FILMED

CONTENTS

1. INTRODUCTION

2. ANALYTICAL BACKGROUND 2

Experimental Arrangement
Theory of T-CHI

3. POSSIBLE MATERIALS 6

4. REFRACTIVE PROPERTIES OF
TGS AQUEOUS SOLUTION 6

Refractive Index n
Calculation of dn/dT at Different Wavelengths
Calculations of dn/dc at Different Wavelengths
Summary of Results for HeNe and HeCd Laser Wavelengths

5. MODELING AND ERROR ANALYSIS WITH SIMPLE
2-D DISTRIBUTION 11

6. MODELING AND ERROR ANALYSIS WITH SIMPLE
ONION-LIKE DISTRIBUTION 13

Introduction
Method
Input Modeling Characteristics
Input Refractive Index Distributions
System Optical Quality Code
Simulated Interferograms
Optical Path Distributions
Two Step Inversion Process
Two Color Holography Sensitivity Assessment
Conclusions

7. BREADBOARD DEFINITION 29

Types of Interferometry
Phase Shift Holographic Interferometry
Design of the Test Chamber

8. CONSTRUCTION OF BREADBOARD MODEL 35

9. DEVELOPMENT TESTS 38

Double Exposure Tests
Real Time Interferometry Case

10. ANALYTICAL EXPRESSIONS TO SUPPORT THE MODELING EFFORT: TEMPERATURE, CONCENTRATION, AND REFRACTIVE INDEX 41

Background
Representative T and C Distribution Expressions
Initial Assumptions
Temperature
Concentration
Refractive Index

11. CONCEPTUAL DESIGN OF A LIGHT WEIGHT, COMPACT, FIBER OPTIC-BASED HOLOGRAPHIC CAMERA SYSTEM FOR STUDIES OF CRYSTAL GROWTH IN SPACE 49

Background
System Design Overview
Component Specifications
Advantages
Technical Considerations and Challenges

12. CONCLUSIONS 58

References 59

1. INTRODUCTION

The Materials Processing in the Space Program of NASA-George C. Marshall Space Flight Center has been active in developing numerous optical techniques for the characterization of fluids in the vicinity of various materials during crystallization and/or solidification.

For example, the Fluids Experiment System (FES) employs holographic interferometry to monitor the solution around a growing crystal. Historically, use of interferometry in low gravity FES began with Mach-Zehnder interferometry dealing with a NASA KC-135 aircraft flying a parabolic trajectory[1-7]. Holographic configurations were also designed, fabricated and tested on such flights[1-2]. Holography is a natural choice for such experiments in space. The main advantage is that reconstructed images can be used for any optical investigation not necessarily interferometry. Storage unit on the flight is only the camera, minimizing the system hardware needs. The other advantage of holography is that very high quality optical components are not needed. Phase errors introduced by imperfect optical components can be cancelled during the reconstruction process. Detailed descriptions of the holographic process and holographic interferometry are readily available[8-11].

Optical holography was chosen as one technique for the Spacelab III Mission. System aspects were considered in detail[12,13]. Ultimately, the holography was successfully performed on the Spacelab III Mission[14,15]. The experiment examined the growth of triglycine sulfate (TGS) crystals in a microgravity environment. Statistical analysis of the system[16], reconstruction techniques of holograms[17] and modelling of the growth[18] and other system aspects[19] are now available.

These successful experiments in space provide new opportunities and challenges. The holographic interferograms yield refractive index variations through the field of interest, i.e. the cell containing TGS solution. The holograms were recorded by a HeNe laser at 632.8nm wavelength. The refractive index variations in these experiments are basically due to concentration and temperature variations in the test fluid. Obviously, the holographic fringes yield the cumulative effect on the refractive index. As such, concentration and temperature cannot be separated. Thermocouples to measure temperature are intrusive. Even so, they are practical at a limited number of points in the test volume.

Now, what about recording two interferograms at two different wavelengths? In principle, by solving two equations, concentration and temperature can then be separated. The concept in the form of a modified Mach-Zehnder interferometer has been developed[20,21]. Applications dealing with heat and mass transfer are also reported[22,23].

In connection with space applications, Ecker et al.[24] proposed the use to two-color holograms for temperature and concentration separation. Experimentation followed at NASA-Marshall Space Flight Center in laboratory as well as on a KC-135 aircraft. These experiments are for succinonitrile-based alloy systems[25-27].

Two-color holographic interferometry[24-27] demonstrates that temperature and concentration separation in transparent (T-CHI) model systems is possible. The experiments were for particular (succinonitrile) systems. Several solutions are possible in Microgravity Sciences and Applications (MSA) experiments on future shuttle missions. Therefore, in this report we evaluate the theory of the T-CHI concept. Although particular cases will be used for explanations, the concepts developed will be universal. A breadboard system design will also be presented for ultimate fabrication and testing of theoretical findings. New developments in holography involving optical fibers and diode lasers will also be incorporated.

2. ANALYTICAL BACKGROUND

This section is devoted to the basic analytical introduction of the T-CHI concept. Starting with the typical experimental arrangement of recording such holograms, the general mathematical formulation will be presented.

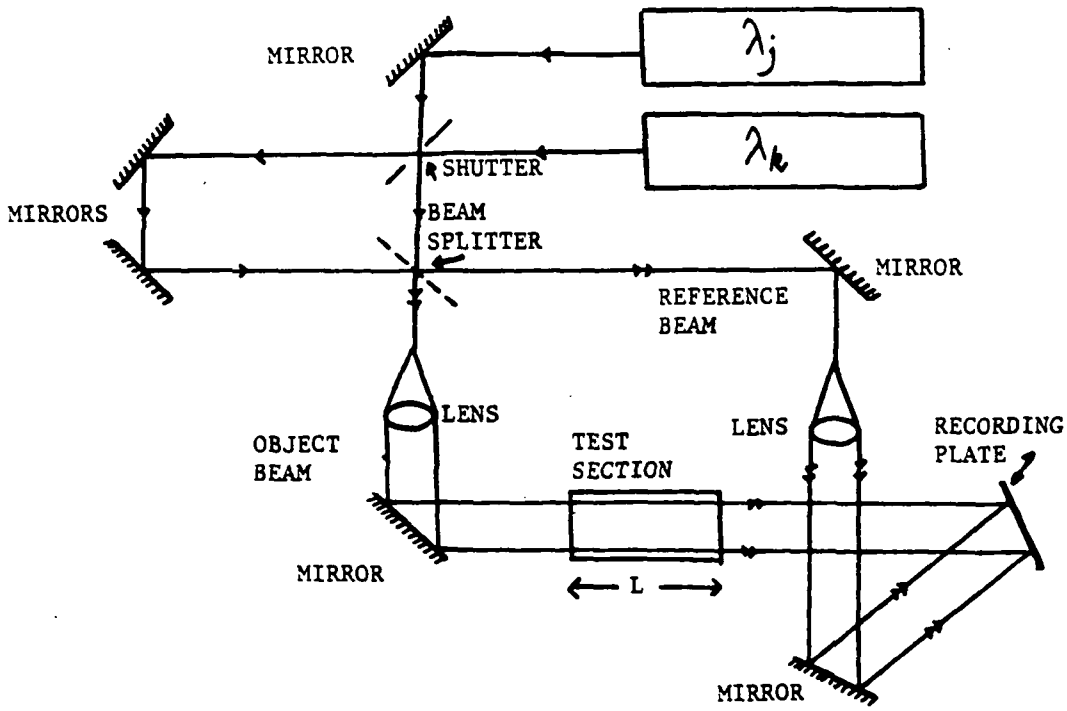

Fig. 1. Schematic diagram of simultaneous recording of two holograms with different wavelengths.

Experimental Arrangement

Figure 1 represents the common experimental arrangement[20-27] of the T-CHI concept. During the recording, two wavelengths λ_j and λ_k can be simultaneously used. During the reconstruction with the reference wave λ_j, the false object wave λ_k is also obtained. However, this unwanted wave emerges at a different angle and can be easily separated. It is better to place the film to face the bisector between the object and the reference beams. This reduces the role of alignment errors and the emulsion shrinkage effects[28]. Regarding the lasers to be used, the wavelengths should be generally as different as possible. Size and weight are also considerations in space applications. The sensitivity of the holographic material (10E75) should be preferably identical. All these considerations lead to HeNe (λ_j = 632.8nm) and HeCd (λ_k = 441.6nm) as suitable lasers[25,26].

Double exposure holograms can be recorded to obtain interference fringes yielding the change in the refractive index between the exposures. The other common approach is to obtain just (single exposure) images and combine them with a collimated plane wave. thus, the resulting fringe pattern yields the desired variation of the refractive index over the test section cross-section.

Thus, two interferograms of the same refractive index variation are obtained. Assuming linearly independent information from these patterns is obtained, concentration and temperature distributions can be separated out. However, regarding the sensitivity and applicability to a particular situation, a careful theoretical analysis is needed.

Theory of T-CHI

When the object beam passes through the test volume, its phase is changed. The optical path length difference of the ray traveling in the s direction through the test volume is[25-29]

$$\Delta\phi = \int_S (n-n_o)\,ds = N\lambda \qquad (1)$$

where n_o is the original refractive index of the phase object and n is the index at the time of the second exposure. If a collimated beam is used to mix with an (single exposure) image to obtain fringes, then n_o is unity. λ is the wavelength of the light used and N is the fringe order. If the refractive index is continuously changing from a reference point (say the crystal surface in a typical growth experiment) then bright and dark fringes will be obtained. These fringes contain information about the refractive index variation. A simple form of Eq. (1) is obtained if the refractive index remains

constant along the propagation direction. If the object wave passes through the length L of the test section, then Eq. (1) in this case becomes

$$(n-n_o)L = N\lambda \tag{2}$$

In this case, the analysis becomes simple. The fringes directly yield the two-dimensional refractive index variation.

In either case, different wavelengths λ will give different fringe patterns. Then it is possible to determine temperature T and concentration C variations. The functional dependence of n on c and T can be represented as

$$n = n_\infty + \frac{dn}{dc}\Delta C + \frac{dn}{dT}\Delta T \tag{3}$$

where n_∞ is the suitable boundary refractive index, and ΔC and ΔT are the respective changes from the boundary point. If the fringes are counted from the boundary point, then the residual fringe order can be omitted. Equations (2) and (3) can then be combined, for wavelengths λ_j and λ_k to yield

$$\frac{N_j\lambda_j}{L} = \left(\frac{dn}{dc}\right)_j \Delta C + \left(\frac{dn}{dT}\right)_j \Delta T \tag{4}$$

and

$$\frac{N_k\lambda_k}{L} = \left(\frac{dn}{dc}\right)_k \Delta C + \left(\frac{dn}{dT}\right)_k \Delta T \tag{5}$$

By knowing the solution properties dn/dc and dn/dT at two wavelengths, the experimental fringe orders can thus yield ΔC and ΔT. This is the basis of T-CHI technique. Equations (4) and (5) can be solved to obtain:

$$\Delta C = \frac{N_j\lambda_j(dn/dT)_k - N_k\lambda_k(dn/dT)_j}{L[(dn/dc)_j\,(dn/dT)_k - (dn/dc)_k\,(dn/dT)_j]} \tag{6}$$

and

$$\Delta T = \frac{N_j\lambda_j(dn/dc)_k - N_k\lambda_k(dn/dc)_j}{L[(dn/dT)_j(dn/dc)_k - (dn/dT)_k(dn/dc)_j]} \qquad (7)$$

The success depends on actual numerical values in Eqs. (4) and (5). At this stage the role of uncertainties of measurements can be introduced. The form of Eq. (4) or (5) directly yields the critical parameters to be considered for the error analysis. For example, the relative error in dn/dc is equivalent to the relative error in ΔC. Similarly, the relative error in dn/dt is equivalent to the error in ΔT. Fortunately[29,30], quantities dn/dc and dn/dT can be measured to about ~ 0.01% accuracy. thus, the role of errors of these quantities can be omitted. The role of impurities on these quantities is beyond the scope of this study and we are considering only the technical capabilities. Now let us consider the role of error in the fringe order. The relative error in N is equal to the relative error in ΔC (or ΔT). It means N must be measured very accurately. Conventional methods leading to fringe order accuracies of 1/4, 1/10 or so are not sufficient. Again, the role of error in L or λ is similar but possible relative error in these quantities is very small.

The above semi-quantitative discussion establishes that the accurate fringe order measurement capability is most important here. Considering this aspect in mind, we are providing here the specific relationship for the errors in ΔT and ΔC. Suppose the lowest fringe order measurement capability is ΔN. Then in Eqs.(4) and (5), N_j and N_k become $N_j \pm \Delta N$ and $N_k \pm \Delta N$ respectively. Solving eqs. (4) and (5) then yield

$$\delta(\Delta T) = \pm \frac{\Delta N[\lambda_j|(\partial n/\partial c)_k| + \lambda_k|(\partial n/\partial c)_j|]}{L[\partial n/\partial c)_k(\partial n/\partial T)_j - (\partial n/\partial c)_j(\partial n/\partial T)_k]} \qquad (8)$$

and

$$\delta(\Delta C) = \pm \frac{\Delta N[\lambda_j|(\partial n/\partial T)_k| + \lambda_k|(\partial n/\partial T)_j|]}{L[(\partial n/\partial T)_k(\partial n/\partial c)_j - (\partial n/\partial T)_j(\partial n/\partial c)_k]} \qquad (9)$$

Here $\delta(\Delta T)$ and $\delta(\Delta C)$ are the uncertainties as compared to the error-free values of Eqs. (6) and (7). So, in a particular measurement accuracy, test chamber depth L, etc. can be determined. These aspects will be considered later in particular numerical situations of actual crystal growth.

3. POSSIBLE MATERIALS

A survey (mainly informal discussions with several scientists associated with crystal growth experiments dealing with NASA) was performed. Out of the suggested materials, the following listed materials are suitable for the T-CHI technique as the solutions are transparent in the visible region.

— LAP
— Urea
— Nh_4Cl
— TGS
— SCN
— Protein Crystals
— KDP
— ADP
— Various dopings of the above.

As seems in Section 2, analysis of the interferograms in the T-CHI technique requires the knowledge of the refractive index as a function of wavelength, temperature and concentration. It was observed that this kind of data is generally not available. Kroes and Reiss[30] have measured the properties of TGS aqueous solution at 589.3nm (sodium vapor lamp). They also found that the index of refraction is 0.0014 lower for 632.8nm (HeNe laser) light in the region of interest. This information and other known analytical relationships helped us to obtain the desired refractive properties of the TGS solution. For this reason, we have used the TGS case as an example in our study. However, the entire analytical base developed in this report is general and can be extended to any other solution of interest. There is no substitute of the actual experimental data. However the analysis of the following section is very useful in the absence of such data.

4. REFRACTIVE PROPERTIES OF TGS AQUEOUS SOLUTION

From the available Kroes and Reiss[30] data, we determine here n, dn/dc and dn/dT at HeNe and HeCd wavelengths. Figure 4 of Ref. [30] concludes that at a given wavelength, dn/dc and dn/dT are practically constant for typical temperature and concentration regions of interest. Thus, the problem left is to determine the refractive index (at a given temperature and concentration) for the other wavelength. Then, we will show later that dn/dc and dn/dT can be determined at the other wavelength. As an example, we are considering 513gm TGS/liter H_2O solution at 45°C. This information is obtained from the solubility curve of the aqueous TGS solution[30].

Refractive Index n

From Figure 4 of Ref. [30], we know the refractive index of 513gm TGS/liter H_2O solution at 589.3nm (sodium vapor lamp) as 1.383298 (we are not rounding the number at this stage).

To determine n under similar conditions but at other wavelengths, Cauchy's equation, i.e.

$$n_\lambda = A + B/\lambda^2 \tag{10}$$

can be used. From the observed value of B and available data[30] one can obtain:

$$n = 1.372753 + 366216/\lambda^2 \tag{11}$$

where λ is in Å. This information of n against λ is plotted in Figure 2.

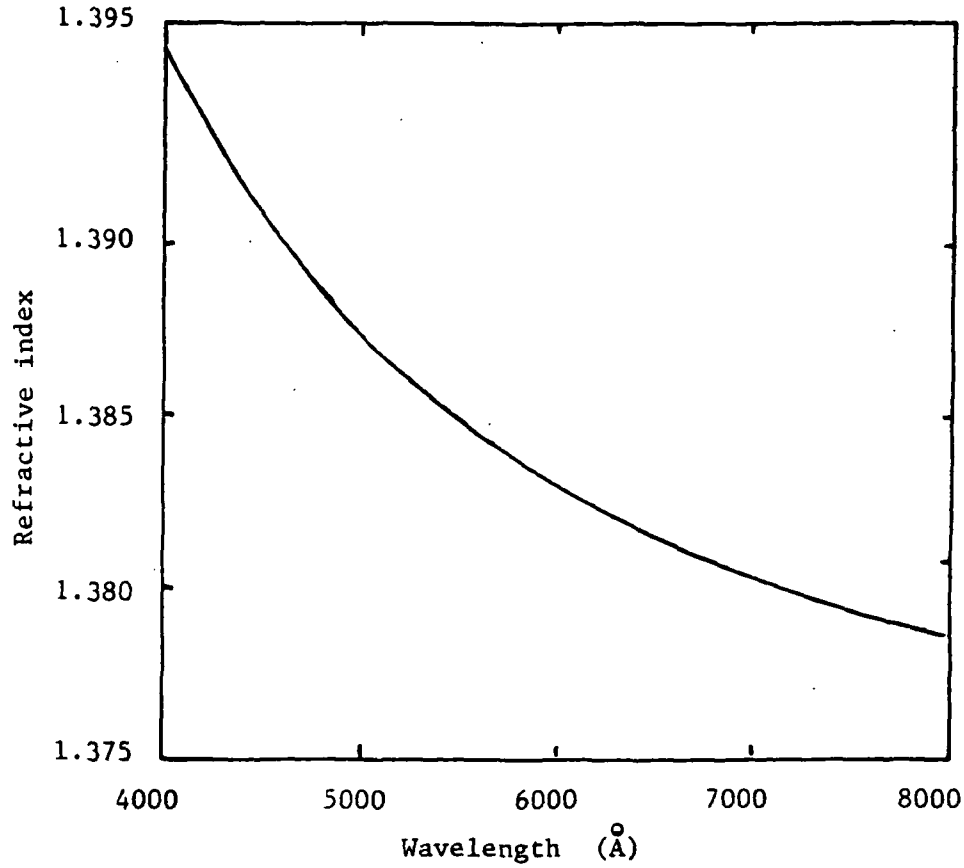

Fig. 2. Variation of refractive index against wavelength for 513 gm TGS/liter H_2O solution at 45°C.

Calculation of dn/dT at Different Wavelengths

When limited data about dn/dT is available, the following relationship[31] is very useful:

$$\frac{dn}{dT} = -\frac{3}{2}\left[\frac{n(n^2-1)}{2n^2+1}\right]\beta \qquad (12)$$

This relationship is accurate to within 2.0 percent. β is the coefficient of thermal expansivity of the liquid. Obviously, β is constant against the wavelength variation. Thus, once dn/dT at one wavelength is known, it can be determined at other wavelengths from the refractive index information of Eq. (11) or Fig. 2. Well dn/dT at 589.3nm for the TGS solution is[30] -0.00020012 $^oC^{-1}$.
So, Equations (11) and (12) yield

$$\frac{dn}{dT} = -7.6443321 \times 10^{-4} \cdot \frac{n(n^2-1)}{2n^2+1} \quad {}^oC^{-1} \qquad (13)$$

The role of this exercise was to eliminate β which is unknown. Equations (11) and (13) can now be combined to determine the value of the TGS solution at any wavelength. The result is plotted in Figure 3.

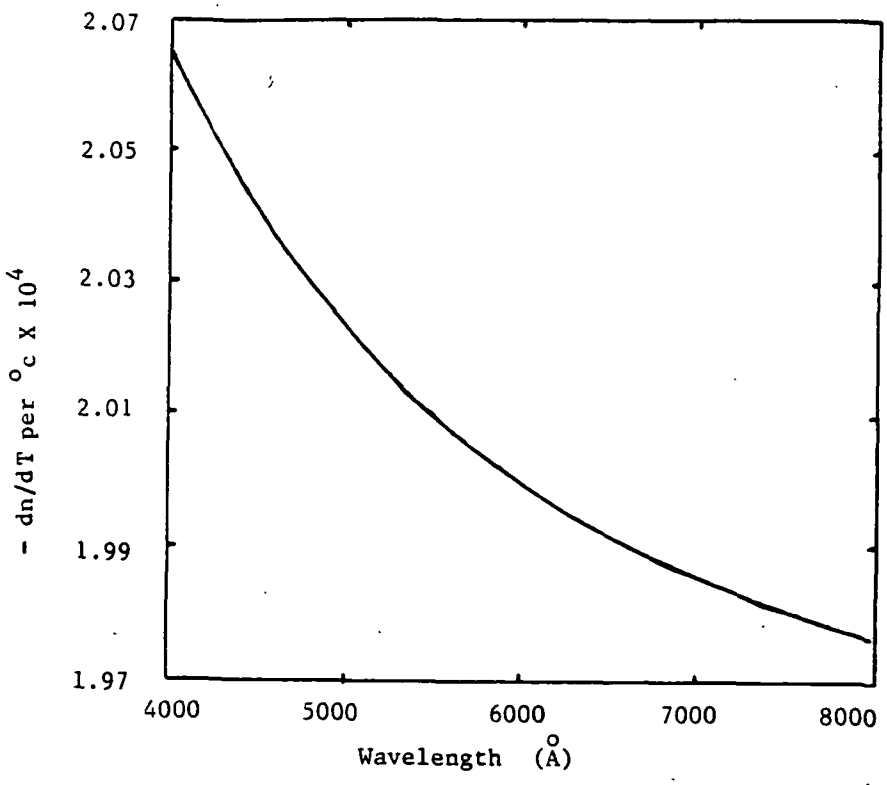

Fig. 3. Variation of dn/dT against wavelength for the TGS solution.

Calculation of dn/dc at Different Wavelengths

In this section we use the Lorentz-Lorenz equation:

$$\frac{n^2 - 1}{\rho(n^2 + 2)} = \bar{r} \qquad (14)$$

where ρ is the density and $\bar{r}$ is the specific refractivity. At a given wavelength and temperature n depends on ρ. Eq. (14) then yields

$$\frac{dn}{d\rho} = \frac{(n^2 - 1)(n^2 + 2)}{6n\rho} \qquad (15)$$

In crystal growth experiments, concentration (c) changes within the cell are very small. Therefore, we can write

$$\frac{dn}{dc} \alpha \frac{(n^2 - 1)(n^2 + 2)}{n} \qquad (16)$$

So, if dn/dc at one n (or λ) is known, it can easily be determined at other values of n. We already know dn/dc of the TGS solution for 589.3nm wavelength as[30] 0.000081682807 (gTGS/liter H_2O)$^{-1}$. Thus, Equations (11) and (16) yield general dn/dc as:

$$\frac{dn}{dc} = 3.16056467 \times 10^{-5} \frac{(n^2 - 1)(n^2 + 2)}{n} \text{ (gTGS/liter } H_2O)^{-1} \qquad (17)$$

Again using Equations (11) and (17), dn/dc against λ is obtained and plotted in Figure 4.

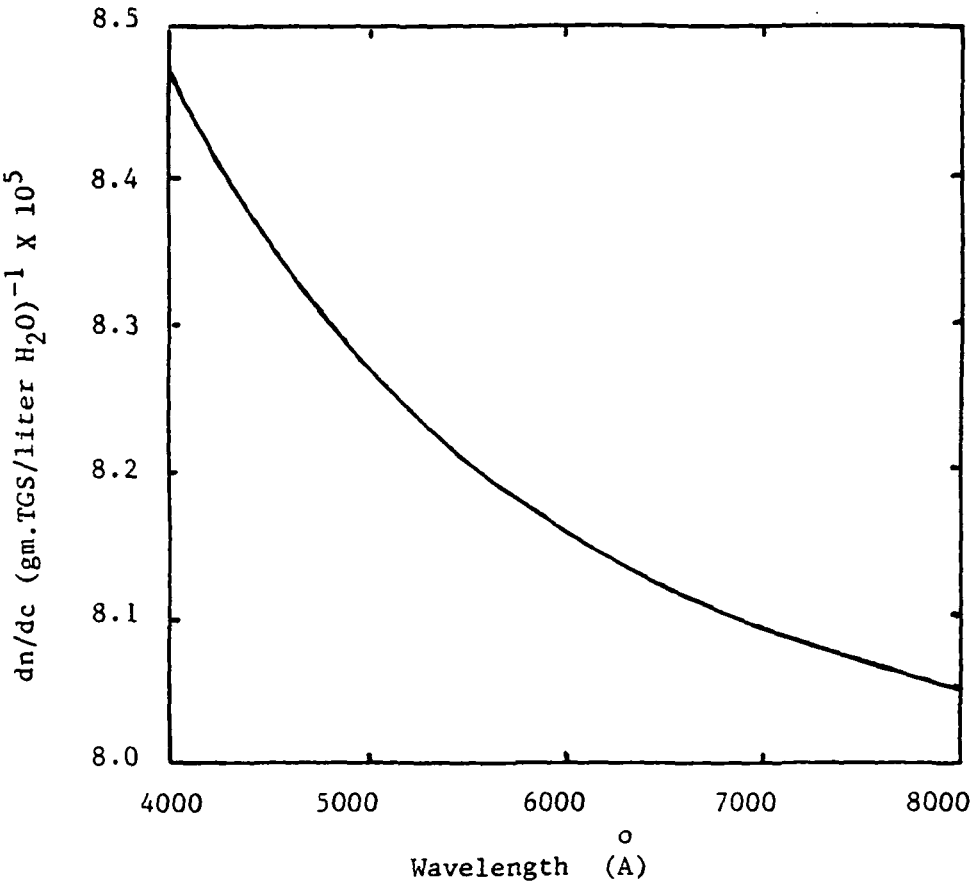

Fig. 4. Variation of dn/dc against wavelength for the TGS solution.

Summary of Results for HeNe and HeCd Laser Wavelengths

In the case of HeNe and HeCd lasers (say j and k respectively), λ_j = 632.8nm and λ_k = 441.6nm. The results of this section can be written in the numerical form (without rounding the figures):

$$\left(\frac{dn}{dc}\right)_j = 0.000081339 \ (gTGS/liter\ H_2O)^{-1}$$

$$\left(\frac{dn}{dc}\right)_k = 0.000083716 \ (gTGS/liter\ H_2O)^{-1}$$

$$\left(\frac{dn}{dT}\right)_j = 0.00019939 \ °C^{-1}$$

$$\left(\frac{dn}{dT}\right)_k = 0.00020441 \ °C^{-1} \qquad (18)$$

5. MODELING AND ERROR ANALYSIS WITH SIMPLE 2-D DISTRIBUTION

We are first considering here the simple cell model where there is no change in the solution along the direction of propagation. This simple model can be characterized by Fig. 5.

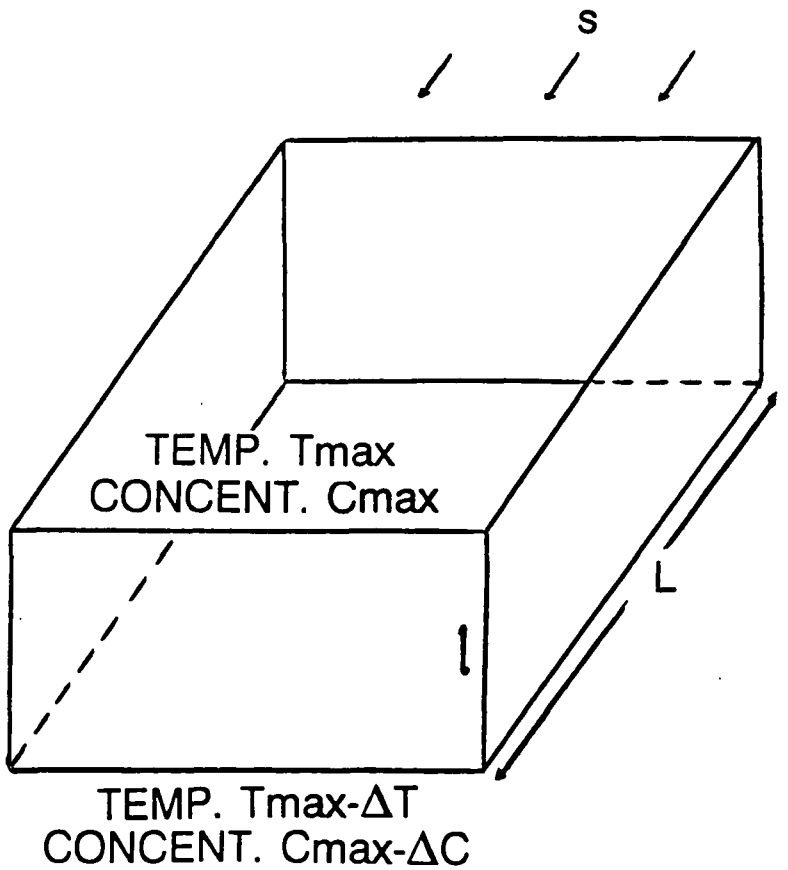

Fig. 5. A simple cell (rectangular parallel piped) describing temperature and concentration variation of a fluid inside.

The solution is in a cell of depth L (i.e. the recording beam passes this length of the fluid) and height l. The temperature and concentration are maximum (for example) on the top of the cell and continuously decreasing to their minima at the bottom. These variations yield interference fringes in the reconstruction. Equations (4) and (5) can be used (along with the data of Sec. 4.4) to calculate the fringe pattern. The result is shown in Fig. 6.

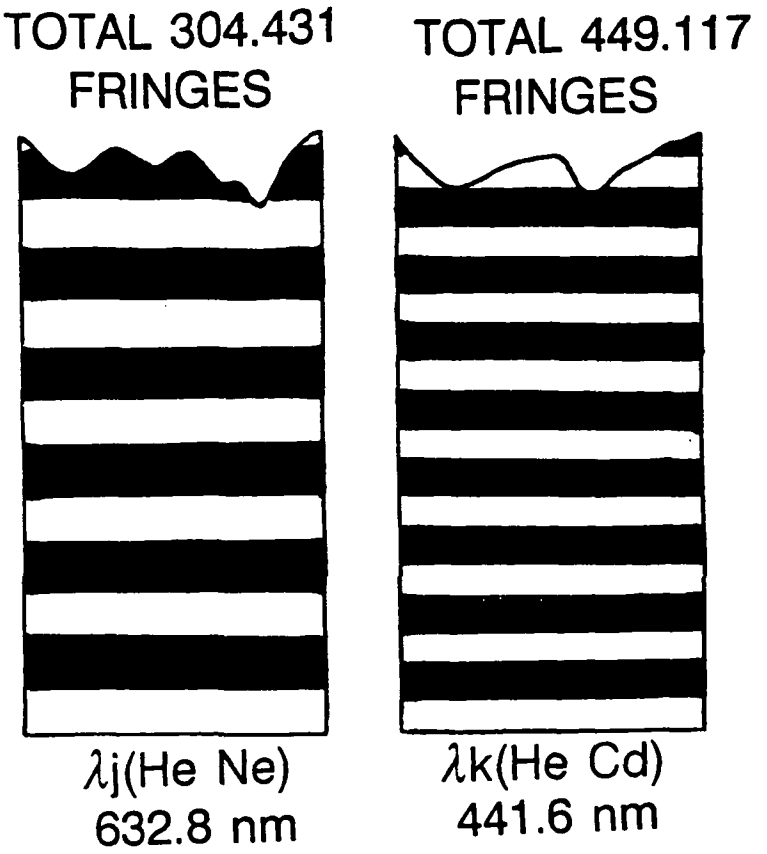

Fig. 6. Appearance of fringes with HeNe and HeCd lasers. The example is for C_{max} = 513 gTGS/liter H_2O solution at T_{max} = 45°C, ΔC = 25.4 gTGS/liter H_2O, ΔT = 0.7°C, l = 5 cm and L = 10 cm.

The numerical values are chosen to be in the range of a typical TGS crystal growth experiment.

In this particular example, Eqs. (8) and (9) yield

$$\delta(\Delta T) \sim \pm 14 \Delta N^{\circ}C \tag{19}$$

and

$$\delta(\Delta C) \sim 33 \Delta N \text{ gTGS/liter } H_2O \tag{20}$$

respectively. ΔN is the fractional fringe order measurement capability. The important outcome is that very small ΔN is required. This aspect has been considered in the breadboard definition and model.

In the next section, we deal with the actual onion-like distribution in detail. Analytical expressions for temperature, concentration, and refractive index in this situation are developed by Metro Laser and described in detail in Section 10. Section 6 is contributed by Teledyne Brown Engineering.

6. MODELING AND ERROR ANALYSIS WITH ONION-LIKE DISTRIBUTION

Introduction

The objective of the modeling of two color holographic interferometry was to validate the two color concept as related to the ability to measure temperature and concentration gradients in a transparent fluid. The physical situation of interest is a crystal growing from solution. The methodology incorporated to perform the optical simulation was derived from the field of modeling aerodynamically-induced optical distortion for the Strategic Defense Initiative. Teledyne Brown's Wave Optics Branch has a wealth of expertise in the aero-optic arena and applied their array of tools to the relatively static situation of crystal growth. The specific pieces of software that were interfaced to complete this task are detailed below. One crystal-specific algorithm was written to generate refractive index information for a wave optics modeling code. Another routine was written to invert wavefront deviations to temperature and concentration distributions. Results at each stage of the analysis are included.

Method

A flow diagram for the two color holographic-interferometric crystal growth analysis is found in Figure 7. Teledyne Brown's System Optical Quality (SOQ) Code was the workhorse for this analysis. The SOQ is a wave optics modeling package originally developed for high energy laser resonator simulations. It was later expanded to facilitate optical analysis tasks ranging from aero optics to optical signal processing. Wave optics provides an exact solution to the wave equation, thereby modeling the diffraction effects that are beyond the capability of ray tracing codes. All software has been rigorously validated. From this SOQ code, sample interferograms, near field phase and optical path distributions were generated allowing temperature and concentration distributions to eventually be derived.

Input Modeling Characteristics

The SOQ code requires definitions of case specific modeling conditions and refractive index information throughout the sample volume, in this case the growth chamber, shown in Figure 8.

Subroutine TGSINDEX was written to establish the optical calculation region's orientation in terms of sample volume coordinates. The grid is positioned normal to the Line Of Sight (LOS) or propagation direction, the y-axis. It maintains this normality throughout the entire propagation. The origin of these coordinates is located at the center of bottom face of the growth chamber, at the crystal. The SOQ grid is a two-dimensional, square, complex array containing 128 x 128 points which stores the details about the optical field.

The calculation region encompasses a 7.5 cm square area. The beam is 5 cm high and 5 cm wide, shown as shaded in Figure 8. The area outside the shaded area is guardband to ensure adequate numerical sampling. The total path for the light to travel is 10 cm.

Input Refractive Index Distributions

Analytic expressions for the fluid temperature and concentration provided by MetroLaser,(see section 10), and UAH yielded the resultant index of refraction at any locale in the sample volume. The theoretical field distribution chosen for this analysis was radially symmetric, or onion-like. Three snapshots were considered at 4, 16, and 36 hour intervals within a total 36 hour growth period. Under these constraints, the analytic description of the temperature, concentration, and index of refraction are defined in Figure 9.

System Optical Quality Code

The SOQ Code performs the propagation of a wavefront through a sample volume applying the effects of the refractive index.

The first step in applying the effects of the temperature and concentration distributions to the optical wavefront is to determine the Optical Path Difference (OPD) induced by the index of refraction for each point in the calculation region. Before performing an actual propagation step, the routine TGSINDEX calculates how far the wavefront can travel through the flow, before accumulating a specified amount of OPD at any point in the optical calculation region.

The routine begins by displacing the SOQ grid a distance along the LOS toward the crystal. The OPD incurred by traveling this distance through the index of refraction is calculated for each point in the SOQ grid using the radially symmetric equations for the temperature and concentration supplied by MetroLaser and UAH. The analytic expressions for temperature, concentration and thus, the index of refraction are computed by subroutine GETINDEX. Subroutine SOQTGS was written to calculate the coordinates of the SOQ point in the sample space and pass GETINDEX the coordinates at which the index of refraction is to be calculated. If a crystal growth density field were provided instead of analytic expressions then a call to a three-dimensional interpolation routine would be provided to extract local index data. A new propagation step is initiated beginning where the previous step terminated. Each propagation step is achieved utilizing a fast Fourier transform that maps the intensity and phase plane to plane, step by step, through the growth chamber.

The output of this numerically intensive procedure is a near field phase distribution. The experimental simulation was run for both Helium Neon (0.6328 microns) and Helium Cadmium (0.4416 micron) wavelengths. The near field phase distribution showed large phase lead at and near the crystal for all simulation times, 4, 16 and 36 hours. The severity of the phase lead will generate high numbers of interferometric fringes. Figure 10 shows an example near field phase distribution for the 4 hour case for both wavelengths.

Simulated Interferograms

A Teledyne Brown internal computer code to generate holograms utilizes this near field phase data to generate sample interferograms detailing the fringe density and shape to be expected for a two color holographic-interferometric experiment. The fringe density was severe in the region just over the crystal. In order to handle this phase variation a small carrier frequency was incorporated into the interferogram to illustrate the fringes. This carrier manifests itself as 200 waves of tilt over the interferogram region. In each case, every tenth fringe is generated and plotted over a 10 cm by 10 cm area. Due to actual growth chamber geometry, the data beyond the 5 cm height is not useful. Fringe

patterns for both wavelengths at each of the three elapsed times were attempted, as shown in Figure 11. The 36 hour Helium Cadmium case had more phase variation than could be plotted with the 200 wave carrier frequency.

Optical Path Distributions

The SOQ was modified to also supply an optical path length topographical map of the wave exiting the sample volume. Optical path fields were generated for both Helium Neon and Helium Cadmium wavelengths and were input to the two color reconstruction algorithm. The optical path fields were numerically subtracted from the reference index to provide optical path difference information. Optical path distributions for the 4 hour simulation follow in Figure 12.

Two Step Inversion Process

The first step towards inverting optical path distributions contained as interferometric data is the generation of wavelength-specific refractive index maps. To accomplish this, an algorithm was written to perform an inverse Abel transform, identified as the Vest Reconstruction Code on the flow diagram Figure 7. This algorithm numerically solves the integral shown in Figure 13, and is appropriate for radially symmetric situations only. The refractive index maps computed are identical in shape and differ only in scale. Each distribution is inverted for data presentation purposes only. The index of refraction is a minimum at the crystal interface. As the distributions show, both temperature and concentration contribute to the net refractive index. The effect of neither constituent can be ignored.

The second step, the Two Color Decomposition Code, solves a system of simultaneous equations (Figure 14), yielding the temperature and concentration at each locale in the sample volume. The analytic and resultant distributions for the 4 hour elapsed growth runs are shown in Figure 14. These resultant fields coincide with the initial temperature and concentration distributions.

Two Color Holography Sensitivity Assessment

The analysis of two color holographic-interferometric sensitivity to wavefront error provided by Dr. Vikram of UAH,(see section 5), is based upon a one-dimensional assumption. This approximation yields a linear relationship between wavefront definition error and index map error. Here the one-dimensional sensitivity study is expanded to that of the two-dimensional onion distribution. Two procedures were followed. First a small temperature displacement added to the temperature equation. The results was a uniform, flat addition to the index of refraction over the entire field. The wave optic analysis was run to generate the optical path displacement distributions. The largest path lead occurs at the crystal interface. This point was tracked and the net change in optical path was logged. This process was repeated to generate the sensitivity curve shown in Figure 15.

The purpose of this study was to assess the sensitivity of temperature change on wavefront definition error. A linear relation exists between wavefront definition and temperature change. Figure 15 shows the temperature sensitivity, or slope, is 1.2 waves per 0.1 ^{o}C of variance. Each wave represents an interferometric fringe. Different wavefront locations, if tracked, would yield correspondingly different slopes, the case reported is the point of greatest sensitivity.

The second sensitivity procedure involves random errors on the order of fringe reduction accuracies and tracks the error effects through the entire algorithm.

A simple algebraic relation between wavefront inaccuracy and index error cannot be derived from the symmetric inverse Abel transform utilized in the Reconstruction Code. The relation is derived by simulation. A random wavefront error of standard deviation was added to one copy of the 4 hour Helium Neon optical path length distribution. The other Helium Neon optical path length distribution was left unperturbed. The Vest Reconstruction Code was run to generate two Helium Neon-specific index distributions one with errors one without. An rms difference of these two resulting index maps was computed. It varied about 5.0×10^{-8}.

The one-dimensional assumption yielded an index reconstruction accuracy of

$$\Delta n = (\lambda/L)\Delta N$$

where Δn is the refractive index variance, λ is the specific wavelength of light, L is the path length and ΔN is the fringe number accuracy. Evaluation of the latter half of this expression yields an index tolerance of 6×10^{-8}. This seems to confirm Dr. Vikram's algebra.

To achieve a +/- 0.1 ^{o}C accuracy in temperature reconstruction, the wavefront should be defined to approximately +/- $\lambda/100$. Again, the 4 hour simulation was chosen for this error analysis. A Gaussian random error of specified standard deviation was introduced to the Helium Neon optical path length distribution. The Helium Cadmium optical path length distribution was left unperturbed. The Vest Reconstruction Code was run to generate two wavelength-specific and erred index distributions. The Two Color Reconstruction Code was run to generate the distributions shown in Figure 16. The analytic reconstruction algorithms produced dramatically perturbed temperature and concentration distributions, (see Figure 16). Smaller deviations of $\lambda/1000$ also yielded similar " poor reconstruction " results.

The source of the numerical sensitivity was traced to the index reconstruction algorithm, labeled Vest Reconstruction Code in Figure 7. The uniform "shift" of the perturbed data with respect to the dashed unperturbed data in Figure 16, is due to the error introduced at the reference point on the perimeter of the field. In short the point chosen as reference may have error associated with it.

A careful analysis of the perturbed map revealed that the error was no longer completely random. Errors in the index map are concentrated in the center of the field and display azimuthal symmetry. This is an artifact of the inverse Abel transform, and could not be predicted by using the one-dimensional sensitivity analysis. Figure 17 depicts the index error as both a two-dimensional map and a one-dimensional normalized slice. Note the symmetry of the pattern as well as the approximate 1/radius weighting of the error distribution. This indicates that the inverse Abel transform distributes the majority of the wavefront inaccuracy in the form of index errors near the center of the field. As this is the region of interest during the crystal growth experiment, it significantly diminishes the quality of the results of this inversion methodology. Figure 16 shows that, upon removing the reference error, a temperature accuracy of +/- 0.1 ^{o}C is observed over most of the field. However, even by increasing the wavefront accuracy requirements to +/- λ/1000, (Figure 16), reconstruction at the center of the field was still inadequate.

Conclusions

A method of analysis has been developed to simulate experimental interferometric results, then process fringe data yielding constituent temperature and concentration distributions of a growing crystal. This was accomplished with a physical optics modeling code, and specialty reconstruction algorithms.

Interferograms were simulated for two colors of light and 4, 16, and 36 hour elapsed times of Tri Glycine Sulfate crystal growth from solution. Once generated the optical path information contained in the interferograms was utilized to decompose optical path into refractive index distributions. These refractive index fields yielded temperature and concentration distributions within the initial growth chamber.

A sensitivity study was performed to connect expected wavefront variations to errors incorporated in resultant temperature and concentration distributions. Optical path differences depicted in Figure 15, show greater optical path sensitivity than predicted by the one-dimensional relation. Discrepancy in sensitivity stems from inherent difference between a one and two dimensional study of this physical situation.

The sensitivity study also revealed that an inversion algorithm which assumes symmetry will not perform well in the presence of asymmetric noise. The effect of asymmetric variations degraded the inverted data and, in the case of random errors, the structure of the calculated distributions was lost. Better reconstruction may be obtained with more powerful asymmetric computer aided tomography algorithms.

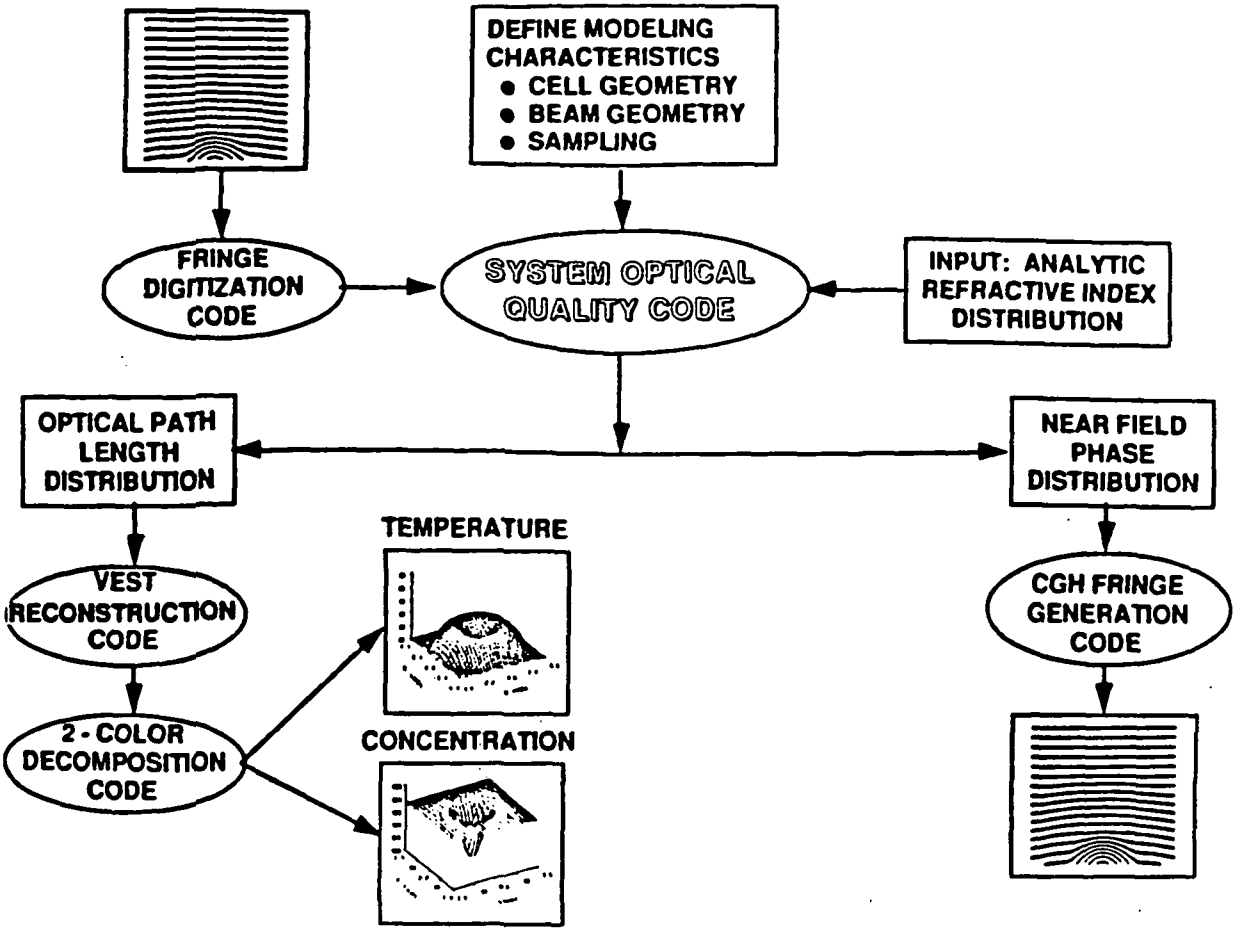

Figure 7. This analytic flow diagram of two color holographic interferometric concept shows component software algorithms, intermediate and final results.

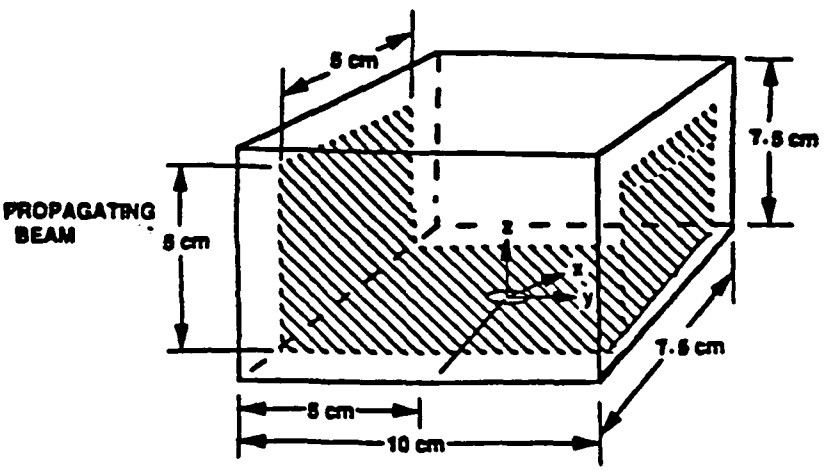

Figure 8. The growth chamber geometry is contained in a rectangular cell. The shaded area covers the traveling analytic beam of light and the origin of the coordinate system is at the crystal.

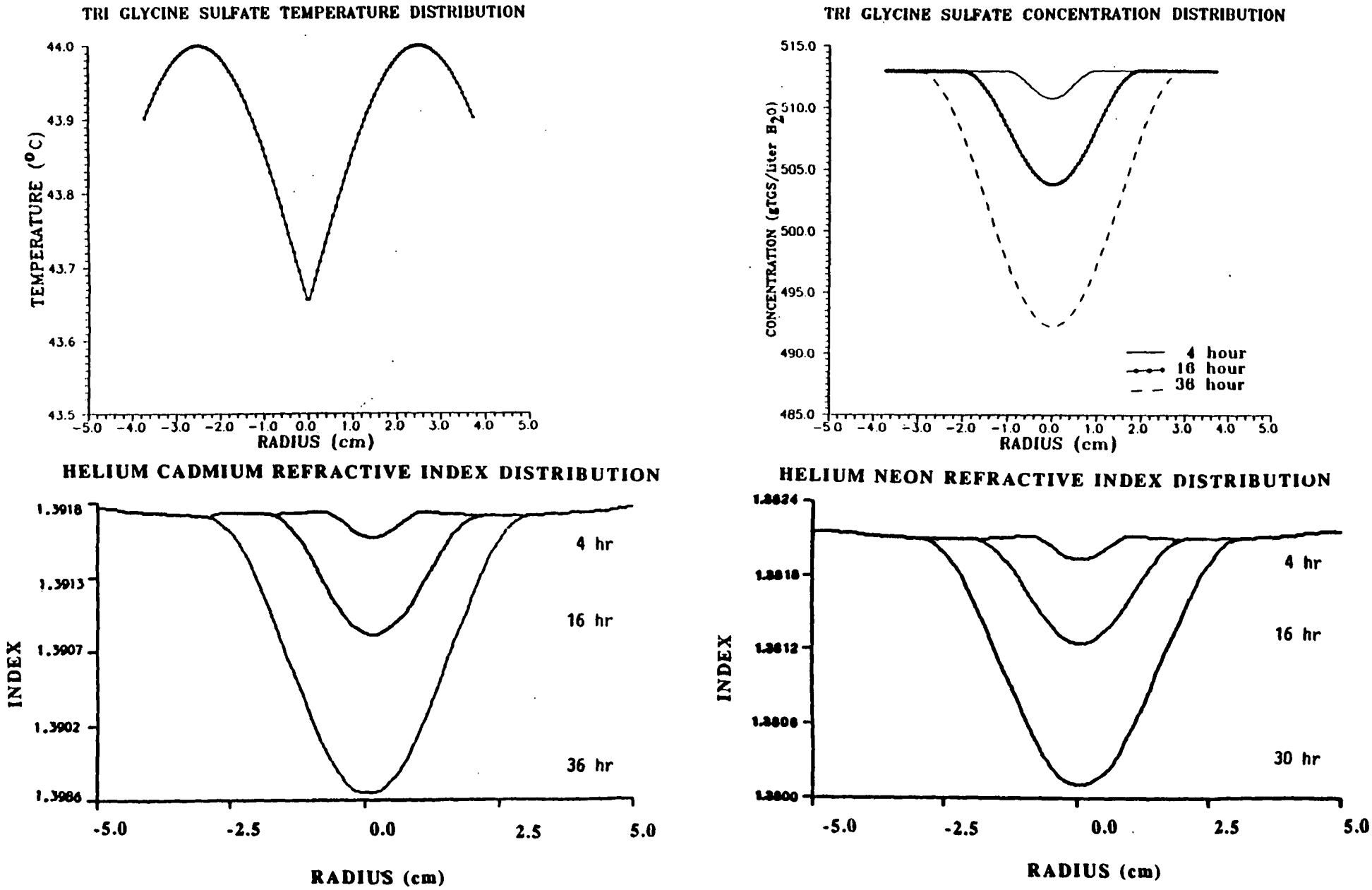

Figure 9. All distributions shown vary with radial symmetry. Temperature varies only with radius. The concentration of TGS is dependent on elapsed growth time. The index of refraction distributions are temperature, concentration and wavelength dependent.

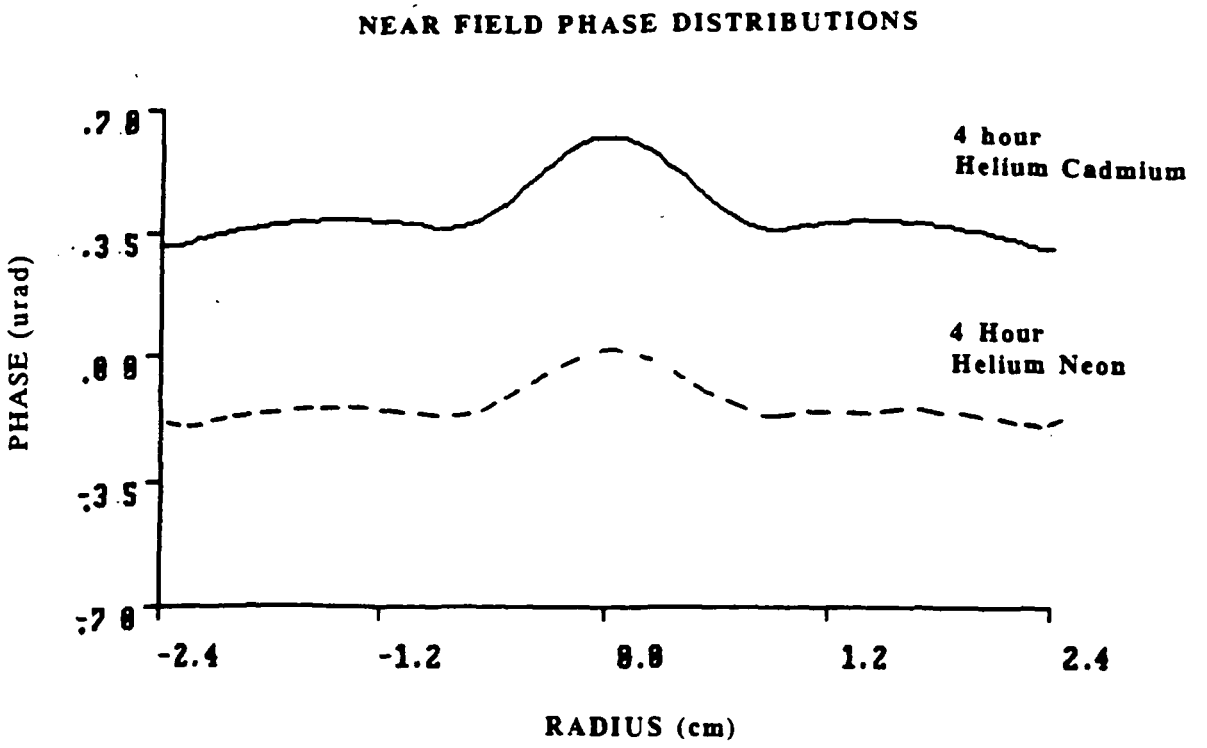

Figure 10. The Helium Neon near field phase distribution lags behind that of Helium Cadmium because of Helium Neon's longer wavelength. The crystal is located at 0.0.

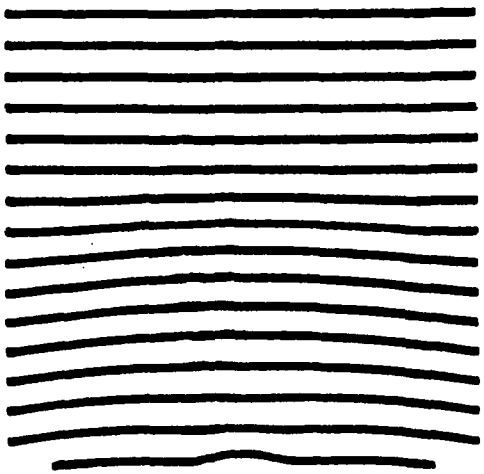

632 nm
4 hour

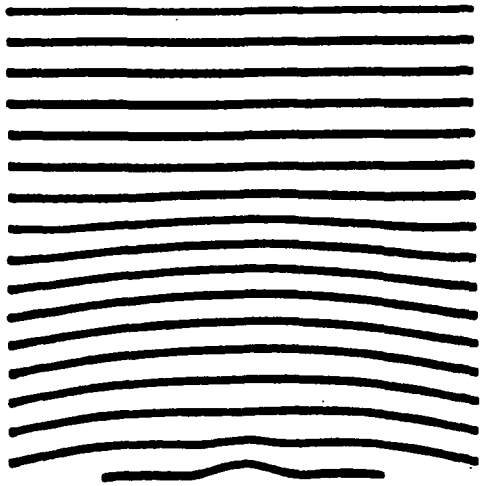

441 nm
4 hour

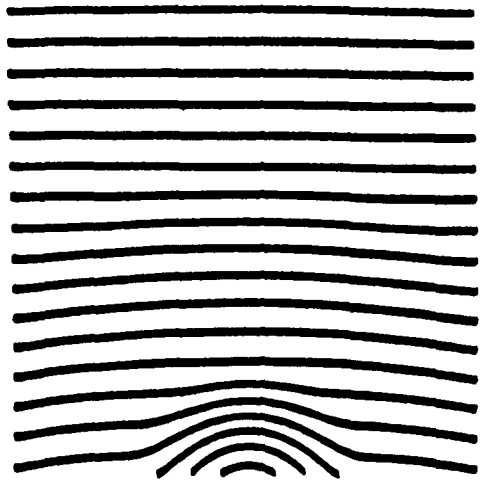

632 nm
16 hour

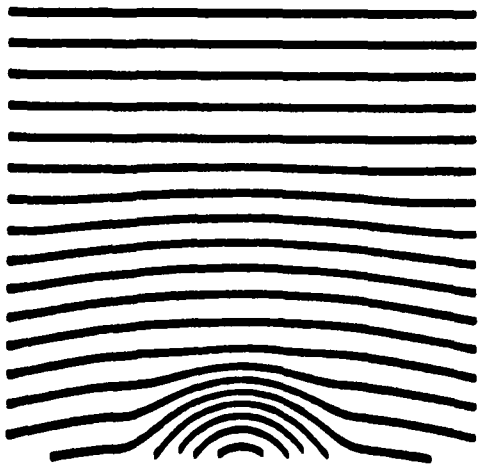

441 nm
16 hour

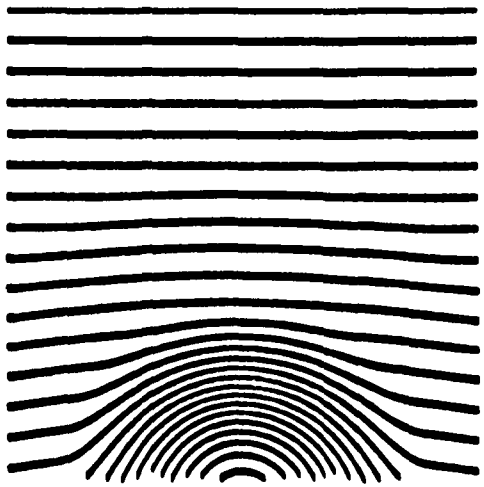

632 nm

Figure 11. Computer generated holographic interferograms show circular contours of refractive index variation about the crystal. Each fringe represents 10 actual fringes.

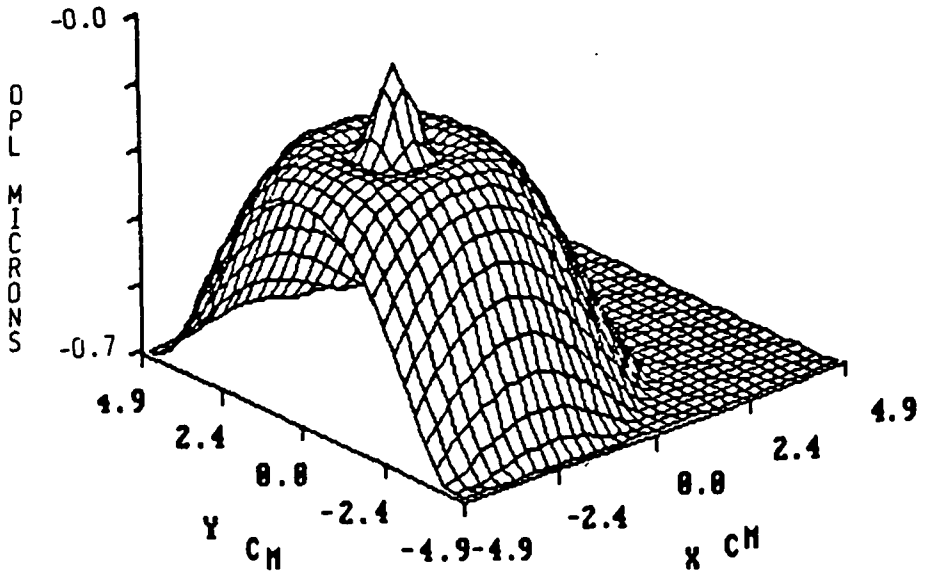

632 nm HeNe

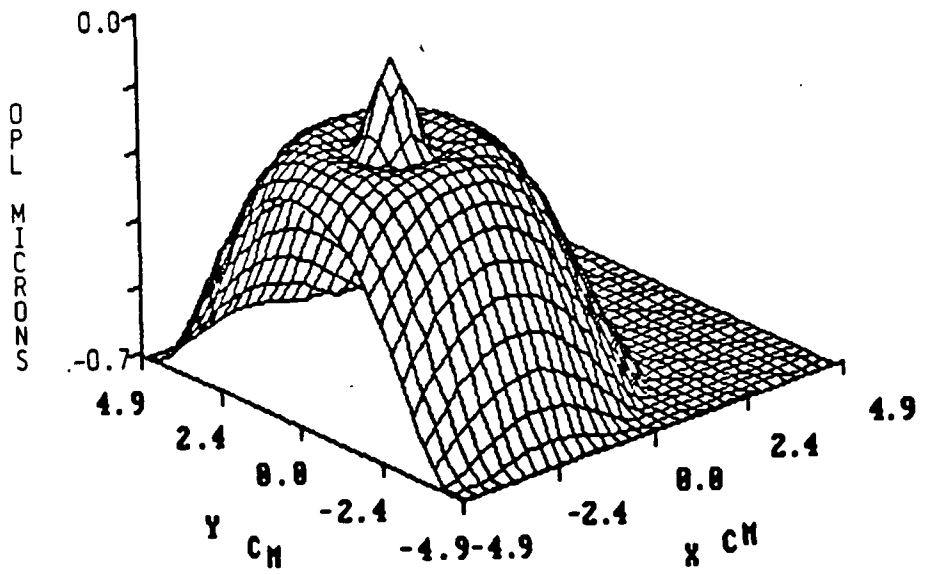

441 nm HeCd

Figure 12. These optical path length distributions are deviations from mean refractive index as measured at the wall. The two maps are identical except for slight differences in scale due to the difference in wavelength.

$$\eta(r) - \eta_o = \frac{1}{\pi} \int_r^{\infty} \frac{(d(OPL) / dx)\, dx}{\sqrt{x^2 - r^2}}$$

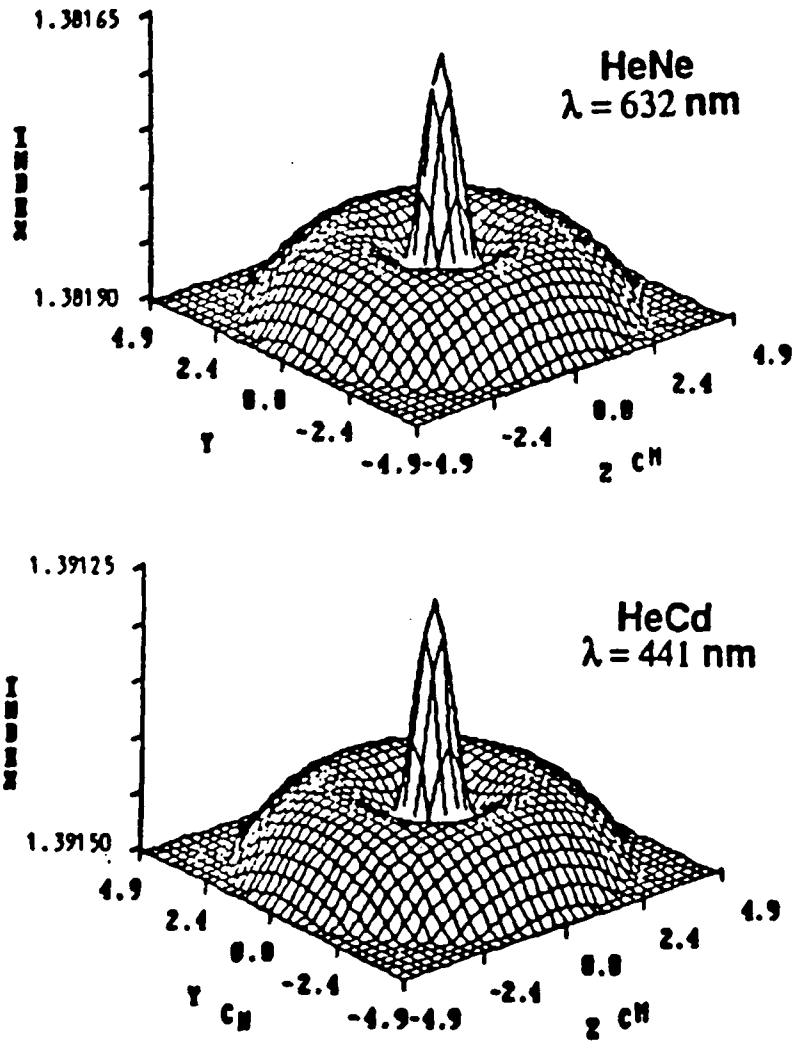

Figure13. The inverse Abel transform is numerically evaluated to generate these refractive index distributions, inverted here for structure clarity. The index of refraction is a minimum at the crystal located at the center of the distribution.

$$\eta_{1o} = \text{EDGE INDEX AT } \lambda_1 = 1.3819 \quad \text{HeNe}$$

$$\eta_1 - \eta_{1o} = \Delta\eta_1 = \frac{\partial\eta_1}{\partial C}\Delta C + \frac{\partial\eta_1}{\partial T}\Delta T$$

$$\eta_{2o} = \text{EDGE INDEX AT } \lambda_2 = 1.3915 \quad \text{HeCd}$$

$$\eta_2 - \eta_{2o} = \Delta\eta_2 = \frac{\partial\eta_2}{\partial C}\Delta C + \frac{\partial\eta_2}{\partial T}\Delta T$$

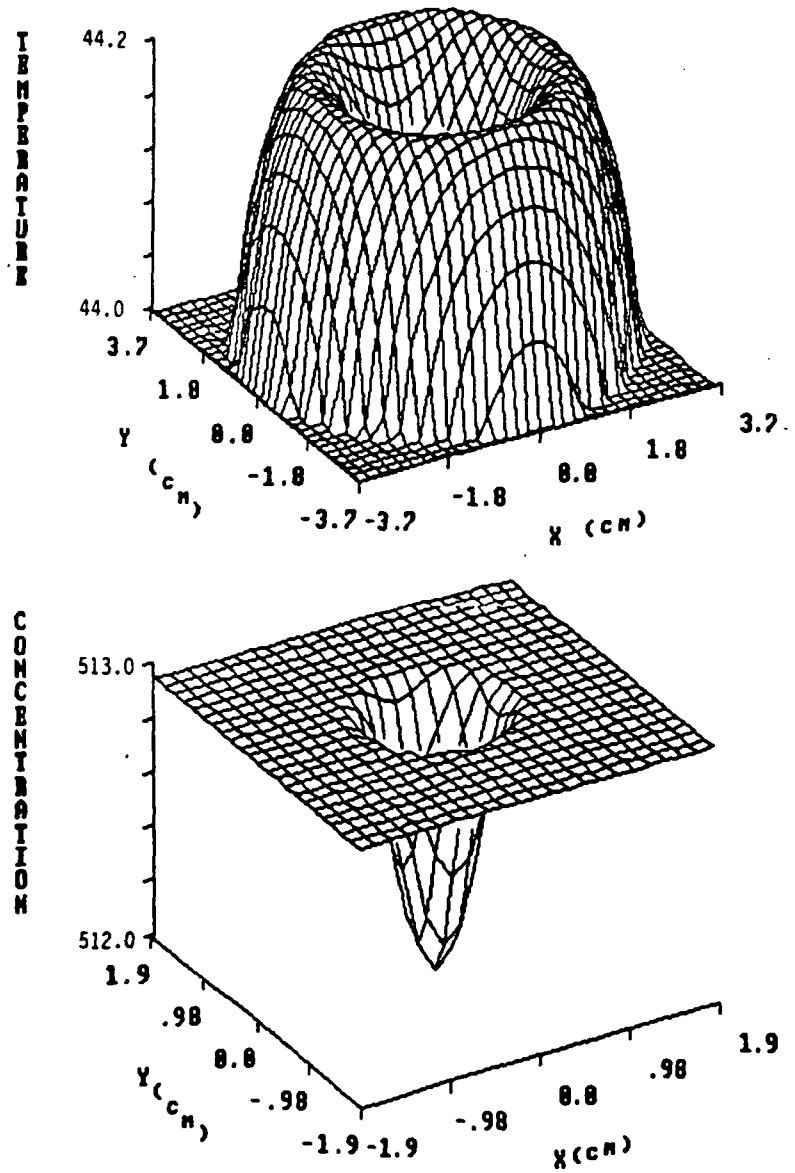

Figure 14. These analytic expressions are evaluated as simultaneous equations for variables Δ C and Δ T.
Temperature,°C, and concentration, gTGS/liter H_2O, are reconstructed given a reference temperature and concentration measured at any point in the field.

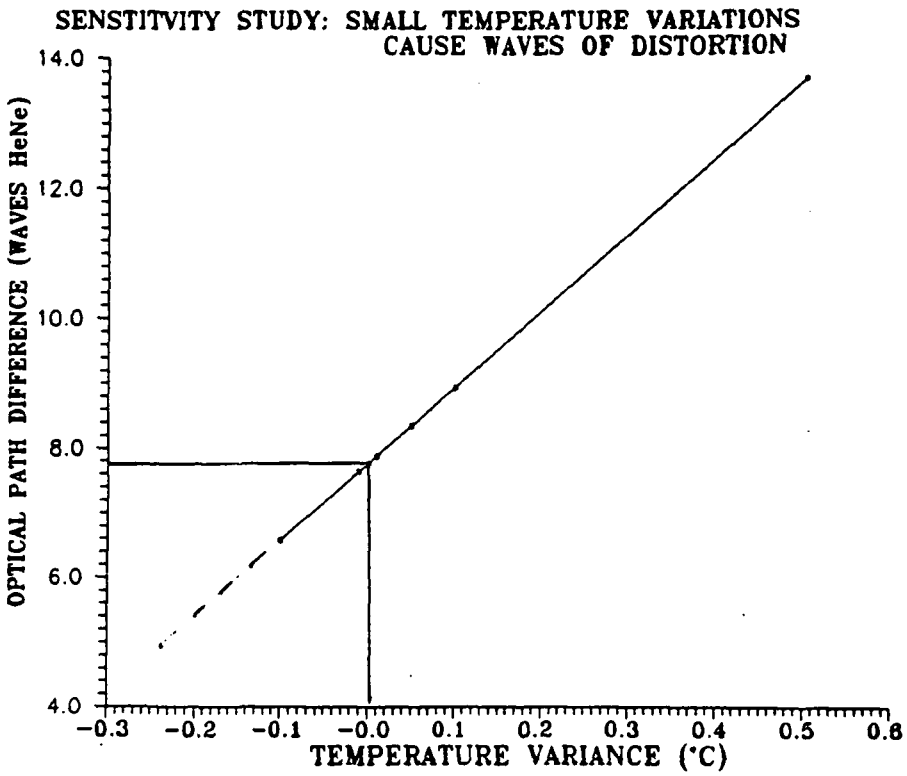

Figure 15. A linear relation exists between wavefront change and temperature variation. The vertical and horizontal lines dictate the wavefront difference associated with the given refractive index, for Helium Neon, at the point in the cell closest to the crystal interface. Temperature variation and corresponding wavefront difference change at a rate of 1.2 waves per 0.1 °C.

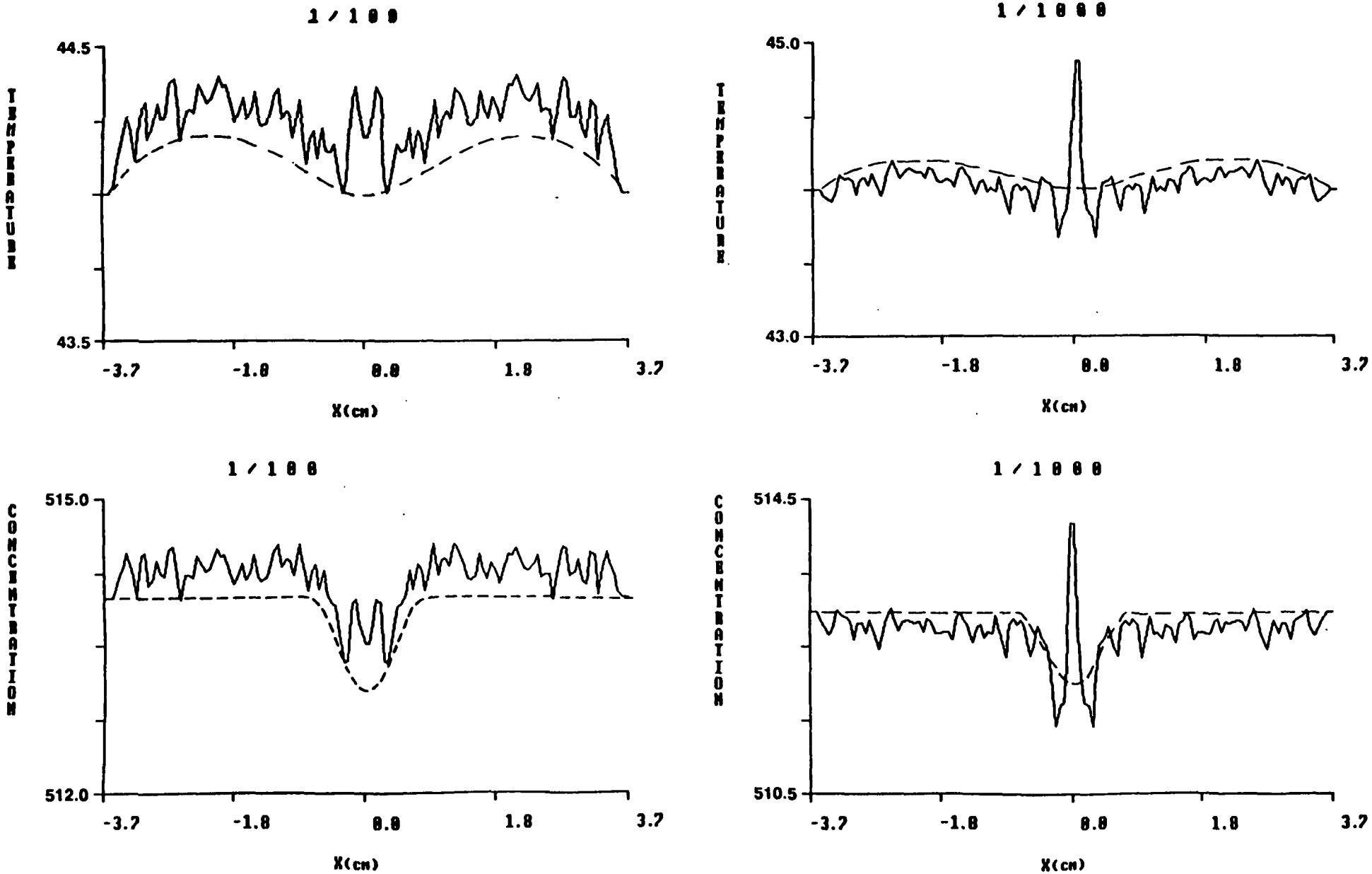

Figure 16. These temperature, °C, and concentration, gTGS/liter H_2O, center slices are reconstructions and represent the results of the analysis. Dashed curves are the ideal and generated from fields without random wavefront error. The solid curve shows the resultant variation that occurs when either $\lambda/100$ or $\lambda/1000$ waves of error are added to the optical path distributions.

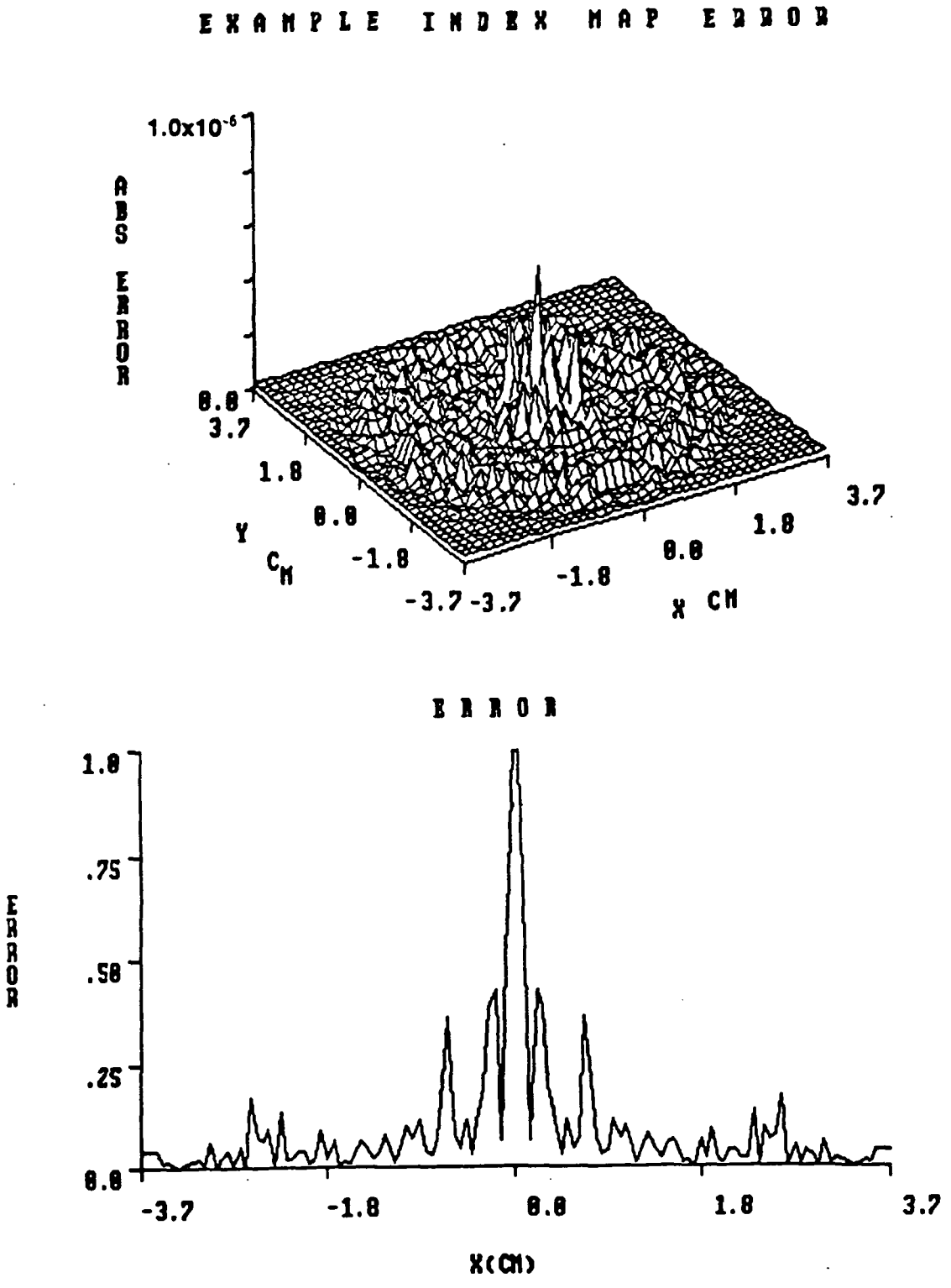

Figure 17. The three-dimensional absolute error distribution is radially symmetric and is associated with reconstruction of $\lambda/100$ waves of Gaussian random error applied to the wavefront. A normalized slice through the center of the error field shows that the error diminishes as 1/radius.

7. BREADBOARD DEFINITION

The last task in the base contract was the design of an experimental apparatus "breadboard" to confirm experimentally what has been shown in the computer experiments and to provide design data for future space flight applications. The breadboard design has several goals in mind:

1. The breadboard must incorporate the capability of accurately duplicating the computer experiments (and vice-versa).

2. A flexible architecture is required to allow advanced study to support an ultimate space flight system design.

3. The experimental cases must be simple enough to reproduce and confirm with accurate supporting measurements but sufficiently complex to incorporate useful test cases.

4. An accurate geometry incorporating simple but meaningful symmetry must be produced.

In the following, these points are treated one by one to explain the evolution of the proposed system.

The experimental breadboard has two independent components, 1) a two (or more) color holographic interferometry system that should be capable of producing high quality holographic interferograms of a field of interest simultaneously at two wavelengths, and 2) a chamber that produces a controllable experiment to provide distributions of temperature and concentration for testing.

The holographic recording system should be capable of producing two holograms simultaneously (one each for two different wavelengths) to ensure that the field is identical for both recordings. Otherwise, a time variation in the field adds still another variable with unknown effects. For convenience and economy, the same holocamera should be useable as a reconstruction system. If the chosen flowfield could be made perfectly stable in time, the simultaneity requirement would be obviated. since simultaneity is not a difficult requirement to fulfill, we chose to make both holograms at once on the same recording.

Hologram quality is important since the technique is under critical evaluation. to allow a poor quality hologram to lead one to the conclusion that the T-CHI technique is not useable would be unfortunate. Therefore, as a baseline case, the highest quality holograms are needed. Consequently, the system should be designed to produce holograms with both the highest signal-to noise ratio and the aberration. The quality of interferograms that ultimately emerge from the holograms should be affected negligibly

or at least in a repeatable manner by the hologram itself; the hologram is only a wavefront recording and storage medium. This can be achieved by employeing the highest quality optics and recording technique that is optimized for the highest signal-to-noise ratio and minimized for aberrations. we have made a careful selection of optics to this end. Also, the tests should be conducted initially on glass-plate photographic emulsion to retain the highest optical quality in the hologram itself.

The experiments should be performed on a table that is sufficiently isolated from vibrations to produce high quality holograms. The need for vibration isolation depends strongly on the type of interferometry and upon required exposure time. The selection of interferometry type is discussed in the next section. For these experiments, the use of real time holographic interferometry could prove extremely advantageous, and this requires fractional wavelength stability. Even though the ultimate space flight system would be designed to require less stability, we recommend that the experiments be conducted on a good quality stable table, to allow complete flexibility.

Figure 18 is a diagram of the proposed holography system

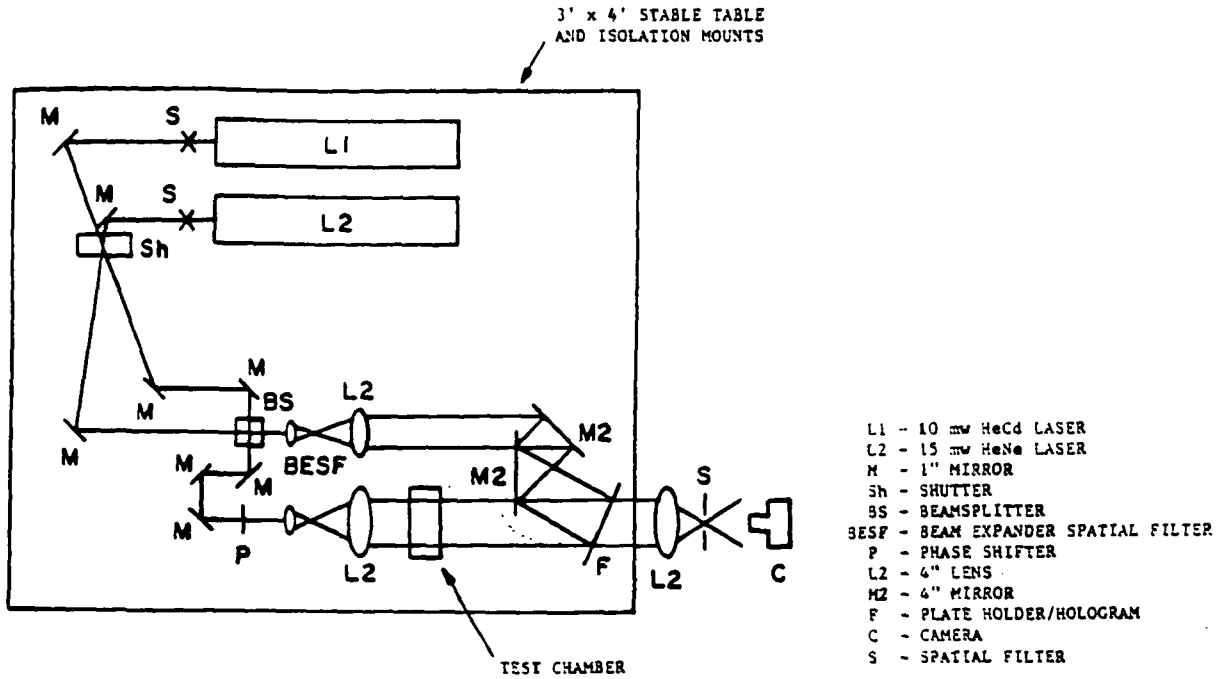

Fig. 18. Proposed T-CHI experimental arrangement.

The system will employ a 10 milliwatt HeNe laser, operating at 633nm wavelength and a 10 milliwatt Helium-Cadmium (HeCd) laser, operating at 442nm. The laser beams will be directed through a common shutter to a pair of alignment mirrors which brings them back to a beam combiner where they are precisely recombined. The mirror pair configuration shown is important to make this alignment practical. One mirror is insufficient to provide both lateral and angular adjustment on such a beam.

Precision alignment capability allows the added benefit of using single spatial filters for both wavelengths. The success of this procedure was verified by Ecker[24-27]. A path matching leg has been added to the object wave. This will allow for the ultimate testing of short coherence lasers that might be advantageous in space flight. The object wave passes through the test cell, described later, onto the photographic plate. At this point the object and reference waves are mixed to form the hologram.

Note that optics are provided to produce the smallest possible reference wave angle. This will allow testing of lower resolution photographic emulsions that might be advantageous for space flight. The T-CHI verification tests will be performed on Agfa 8E75 holographic plates. This angle should be set at about 30 degrees for the best results.

Although it could be advantageous for some experiments to separate the two reference waves into two angles, we see no advantage for this in this program. Therefore both reference waves strike the hologram at the same angle.

The hologram can be returned to the same plate holder after processing so that the recording system can be used also as a reconstruction system. After the hologram, an imaging system is designed to allow a recording camera to focus on the center of the test cell and also to act as a spatial filter to separate the two images that will be formed at each wavelength. Since two holograms exist on the same plate (one for each color), two images will result with one being the correct, desired one and the other being a parasite image propagating outward a different angle from the hologram. The parasite image is easily removed in this way.

Finally, a standard 35 millimeter camera will be used to record the interferograms.

We also recommend that the existing NASA holographic data reduction station be used to assist with data reduction. The system can be used either to reduce data from the recorded photographs or the image can be reconstructed directly into the existing NASA system. The use of the existing hardware will prove highly cost effective.

Types of Interferometry - So far the discussion of the hardware has centered on the need to produce high quality holograms and on flexibility to allow testing of advanced concepts. The type of holographic interferometry to be used has not been discussed. Of the various types of interferometry that could be employed, we believe there are

three methods that should be incorporated into the system:

1. Double exposure
2. Real time
3. Phase shifting

The first method, **double exposure holographic interferometry**, is perhaps the simplest and has been used by most of the references reviewed. In it, a hologram is recorded to serve as a reference, and a second recording of the field of interest is then superimposed on the first. This provides a direct measure of phase shifting caused by the change in the object. The experiment should be stable to a fraction of a wavelength between recordings. The greatest disadvantage is that a separate hologram must be made for each condition of the object. Also, what is actually measured is the change in phase that occurred in the time that passed between the making of the two recordings. The data exists in the form of interference fringes wher the deviation of these fringes from their initial position provides a measure of pahse change. Exce[t for the first recording, which compares the initial condition with the later condition, this is not the simplest data to interpret. that is, the measurement being made is a time derivative of a spatial derivative, instead of an absolute quantity.

The most common data reduction method is to locate fringe centers which are the contours of equal phase shift through the field of interest. A final choice between two methods, finite fringe interferometry and infinite fringe interferometry, must be made. the former is most useful when the total fringe shift in the light wave is less than one wavelength. This requires a small tilt ot be added to either the object wave or the reference wave after the first exposure is made, to bring about a reference set of fringes in the interferogram. ONe disadvantage to this type of data reduction is that data is provided only on the fringes, leaving gaps that must be interpolated between the fringes.

For theoretical comparisons, a comparison of the initial condition with the final condition would be more appropriate. Also, many such comparisons would improve the results. This is possible using **real time interferometry**. In fact, real time holographic interferometry, being much more versatile, is widely used ot evaluate holography applications and to select the optimum type of interferometry. The "live" fringes are observed dynamically and, as the object evolves, an essentially unlimited number of interferograms can be recorded providing a complete time record of the condition of the object.

The main disadvantage of the real time holographic interferometry is that an interferometrically stable table is required for the experiment. This presents little problem in a laboratory environment, but in a field environment can creat considerable difficulty. We believe that its versatility justifies it s principal use in this program.

Phase shift holograpic interferometry is a relatively new method that employs sequentially known phase shifts to move fringes in the interferogram in an advantageous way. This can lead to much higher accuracies in phase measurement (over an order of magnitude). The data reduction can be accomplished in a variety of ways. For example, by making two known phase shifts to produce effectively three independent interferograms, the interferometry equations of three variables are solvable for phase by simply measuring intensity in the interferograms. alternatively, fringe centers can be positioned at any desired place on the interferogram. Therefore, ono interpolation is necessary, and much more data is available. Consequently, accuracy can be greatly improve. We believe that the incorporation of the capability of phase shift interferometry into the experiment may be of critical importance for some of the cases of interest where accuracy and spatial resolution are important.

Therefore, in the proposed system we have incorporated a phase shifting element in the reference wave to allow for this possibility. The phase shift procedure can be used with either double exposure or real time interferometry. However, it will prove most effective with real time interferometry, since here it is easier to produce the additional interferograms.

Design of the test chamber - If the relationship for refractive index and its dependences on temperature, concentration, and wavelength were accurately known, and if the quality of interferogram produced in an experiment were known, we should ask what is the purpose of performing this experiment. We do not need to question whether interferometry works to produce phase shift measurements. We know that conventional interferometry provides phase shift measurements to approximately 36 degree accuracy (1/10 of a fringe shift sensitivity). We know, too, that new techniques can extend this by over an order of magnitude.

When refraction is no longer negligible in interferometry, phase determination becomes much more difficult. We can easily determine from an interferogram when refraction is important. In the jamority of cases of interest, over most of the field of view in the present case, refraction is not important. The solution of the problem of phase shift determination when refraction is important should be treated separately as another technique development, when and fi applications requiring it emerge, because this is an extremely complex problem with no single solution.

We know that if we have two independent equations with two unknowns we can solve them. So if the relationship for refractive index and its dependency on temperature, concentration, and wavelength were accurately known, and if the quality of interferogram produced in an experiment were known, what is the real requirement of the experiment? The answer is that the sole purpose of the experiment is to qualify these assumptions in theoretical analysis. This will provide a final validation, qualifying, and bounding of T-CHI and will provide a demonstration in a real experiment.

Therefore, the design of the test chamber and the experiments to be run are extremely important. If a complex distribution is sought, what we will be testing is not T-CHI, but our ability to match the theoretical and experimental case. what is needed is an experiment that provides the simplest and most accurately controllable geometry and provides the widest range of variation of conditions.

We have included the foregoing discussion of the experimental philosophy to prepare the reader for an almost trivially simple but unique test chamber that meets the above requirements. The test cell is shown in Figure 19.

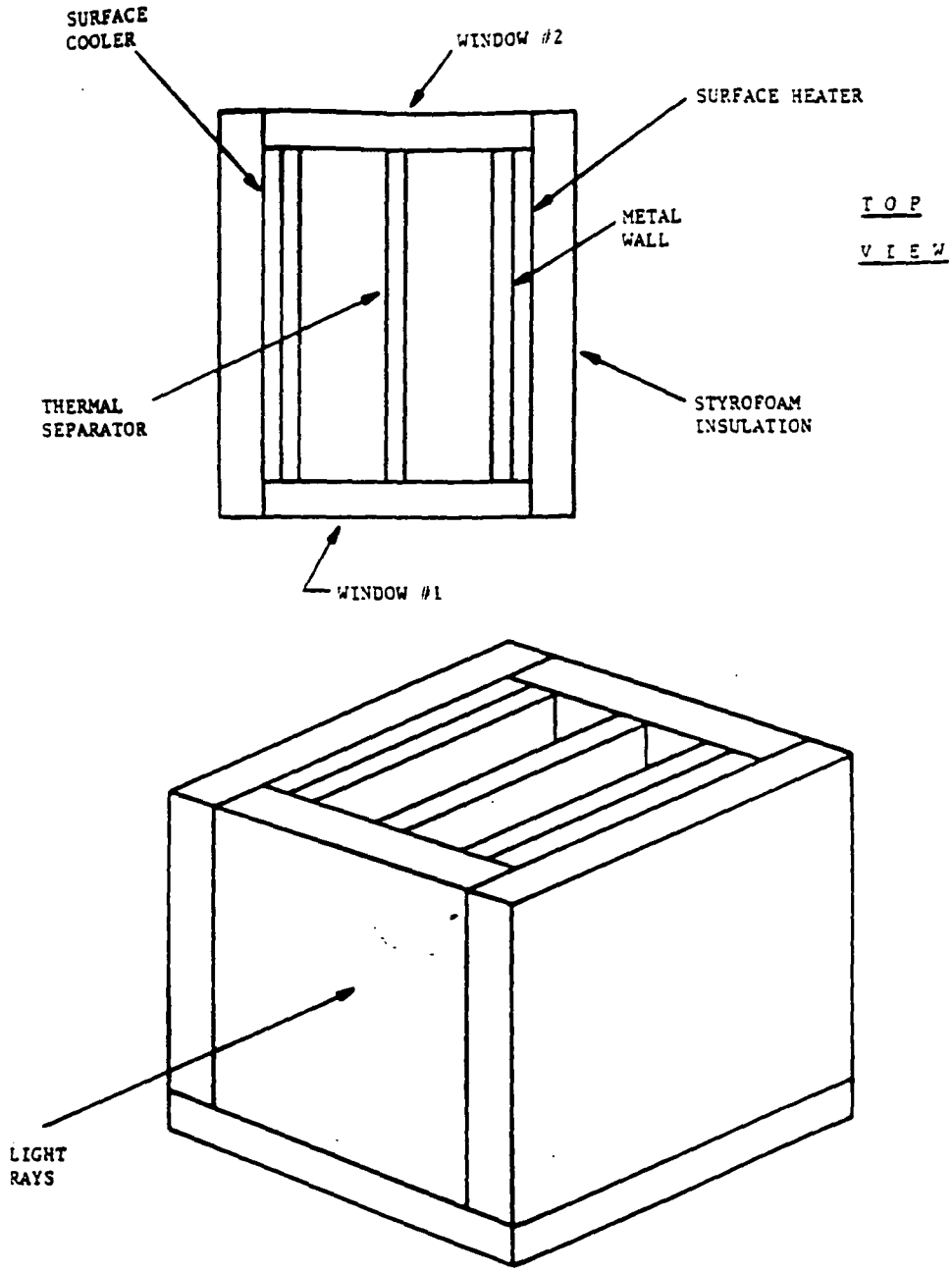

Fig. 19. Schematic diagram of the test cell.

The cell comprises two thermally separated chambers positioned in close proximity. The fluid in each chamber will be temperature controlled by a thermistor, heater and/or cooler, and a stirring device to ensure uniform temperature. The thermistor will provide an accurate temperature record. Since two completely different fluids can be placed in the two containers, complete control can be maintained over the parameter of concentration. In this simple arrangement two fluids of selectable, uniform concentrtion and selectable, uniform temperature can be placed adjacent to each other to determine the phase shift introduced on a light wave of a specific wavelength and a selectable path length. This is precisely what is required to test the ability of T-CHI to separate the phase shifting effects related to T and C.

Fringes will be generated in the interferogram using finite fringe interferometry. This requires a tilt to be added to either the object wave or reference wave for the second exposure. This will be achieved with the phase shifting device shown in Figure 18. Either double exposure or real time interferometry can be used. Horizontal fringes will cross over the two chambers continuously until a change is made in the refractive index in either cell.

The anticipated data appearance, test matrices, and data reduction will be discussed in Section 9.

To provide a demonstration of a more complex distribution of T and C in a single interferogram, the same hardware can be used to provide temperature control of a fluid between two horizontal plates. In thsi way a linear variation in temperature with vertical distance at a fixed concentration can be provided. The gradient can be set by varying the temperature difference between the two plates. The concentration can be varied by adding solute to the fulid. The only apparent objective that such an experiment adds is the demosntration that a linear temperature gradient can be generated. The system will be designed to accommodate such an experiment in case the theoretical study of the base contract determines its necessity.

8. CONSTRUCTION OF BREADBOARD MODEL

Except for the test cell, all components in the system will be commercially available components.

The following table includes a listing of the optical components required for the proposed system, and a breakdown of their cost:

Table 1. Optical Components

Component	Quantity	Cost ($)
1 inch Dielectric Mirror	10	1000
4 inch Mirror	3	1860
Automatic Shutter	1	750
50% Beamsplitter	1	100
Laser Spatial Filter	2	340
Image Spatial Filter	1	340
Lens	4	100
Phase shifter	2	200
Plate Holder	1	475
35 mm Olympus Camera	1	400
10 mW HeNe Laser	1	4400
10 mW HeCd Laser	1	7750
Remote controlled rotary mount	1	2000
	Total	19715

The following Table provide a listing of the proposed mechanical mounting components, and a breakdown of their cost. This includes a part to hold each optical component and to fasten it to the stable table:

Table 2. Mechanical Mounts

Mounts	Quantity	Cost ($)
Steerers	2	1700
Mirror (Small)	6	1800
Mirror (Large)	3	1200
Laser	4	400
Shutter	1	200
Beamsplitter	1	300
Spatial Filter	3	300
Lens	4	200
Phase shifter	1	1100
Plate Holder	1	300
Camera	1	300
Test chamber	1	400
3'x 4' Bread board/stable table	1	3260
	Total	11460

The test chamber must be specially constructed. As described in the last section, there will be three chambers that can be used in a variety of configurations. Two of the three chambers will be identical. When used together, the two identical chambers will sit side by side and the controllers will maintain uniform, time variable temperature in each chamber. For this case, therefore, two contiguous regions with different with regions with different concentrations and variable temperature will be employed to observe the effects on an interferogram as described in the next section.

The third chamber will be used to produce a spatially varying temperature with a constant, uniform concentration. The temperature controllers used in the two identical chambers have been selected so that they can also be used to produce a linear temperature variation between two horizontal plates. The plates must be long compared to their separation to render the end effects negligible. Table 3 lists the components selected for the test chamber, and their approximate cost:

Table 3. Test Chamber Components

Component	Source	Cost ($)
1" x 3" x 6" (two)	Specially constructed	4000
1" x 3" x 6"	Specially constructed	2000
Thermistor (two)	Omega	600
Heater(one)	Omega	300
Cooler(one)	Omega	400
Stirrer(two)	Omega	200
holographic plates	Agfa	200
film	Kodak	50
	Total	7750

To accommodate tests of advanced techniques that should be considered for a space flight system (discussed in detail in Section 11), a number of additional components are required. These will not be used for the primary evaluation of T-CHI for the reasons cited above. This hardware is to accommodate the testing of fiber optic holography, solid state laser diodes, and phase shifting interferometry. The testing of fiber optic holography is easy to plan in the option contract, and we propose to perform such tests. Also, the testing of the laser diodes is proposed. To propose a test using the YAG laser (required to get the shorter wavelength) is more difficult. This technology is in a rapid state of development. such a laser is relatively expensive today. Also, laser diodes operating at shorter wavelengths may be available for these tests within a year. Therefore, we have not proposed acquiring the YAG laser in this proposal.

9. DEVELOPMENT TESTS

Much of the discussion of testing was required to define the design of the breadboard model in Section 7. therefore, in this section, the test matrix and the anticipated appearance of the data will be emphasized.

The following test procedure will be repeated for a number of materials of interest to the Materials Processing in Space Program:

Double Exposure Tests

1. The two identical test chambers will be placed side by side in the field of view of the holocamera.

2. Known concentrations of the solution will be placed in each cell, beginning with zero concentration in both.

3. A hologram will be made at both wavelengths simultaneously.

4. A tilt will be added to the object wave sufficient to produce at least two fringes in the interferogram. A 100 microradian tilt will produce finite reference fringes separated by 0.6 centimeters. This is achieved by adjusting the phase shifting element with the remote control rotary mount. The tilt will be selected so as to make the fringes run normal to the adjacent cell walls, thus crossing over both cells.

5. A second exposure is then added to the hologram at both wavelengths. The holographic interferogram is thus produced.

6. The interferogram is reconstructed into the 35 mm camera first at one wavelength and then at the other and recorded in each color. The fringes in the data should have the appearance shown in Figure 20, running continuously across the image of the two cells.

7. The temperature in one of the cells will then be increased by an amount required to increase the optical path through the cell by less than one wave. The reference fringes in the interferograms resulting from a repetition of the above steps will shift in the cell with increased temperature. The data will take on the appearance shown in Figure 20. This provides an interferogram that can be tested for measuring temperature effects alone.

8. The next step is to vary the concentration of the solute to examine the same effects on phase shifting or refractive index of the fluid. A similar effect on the interferogram is shown in Figure 20.

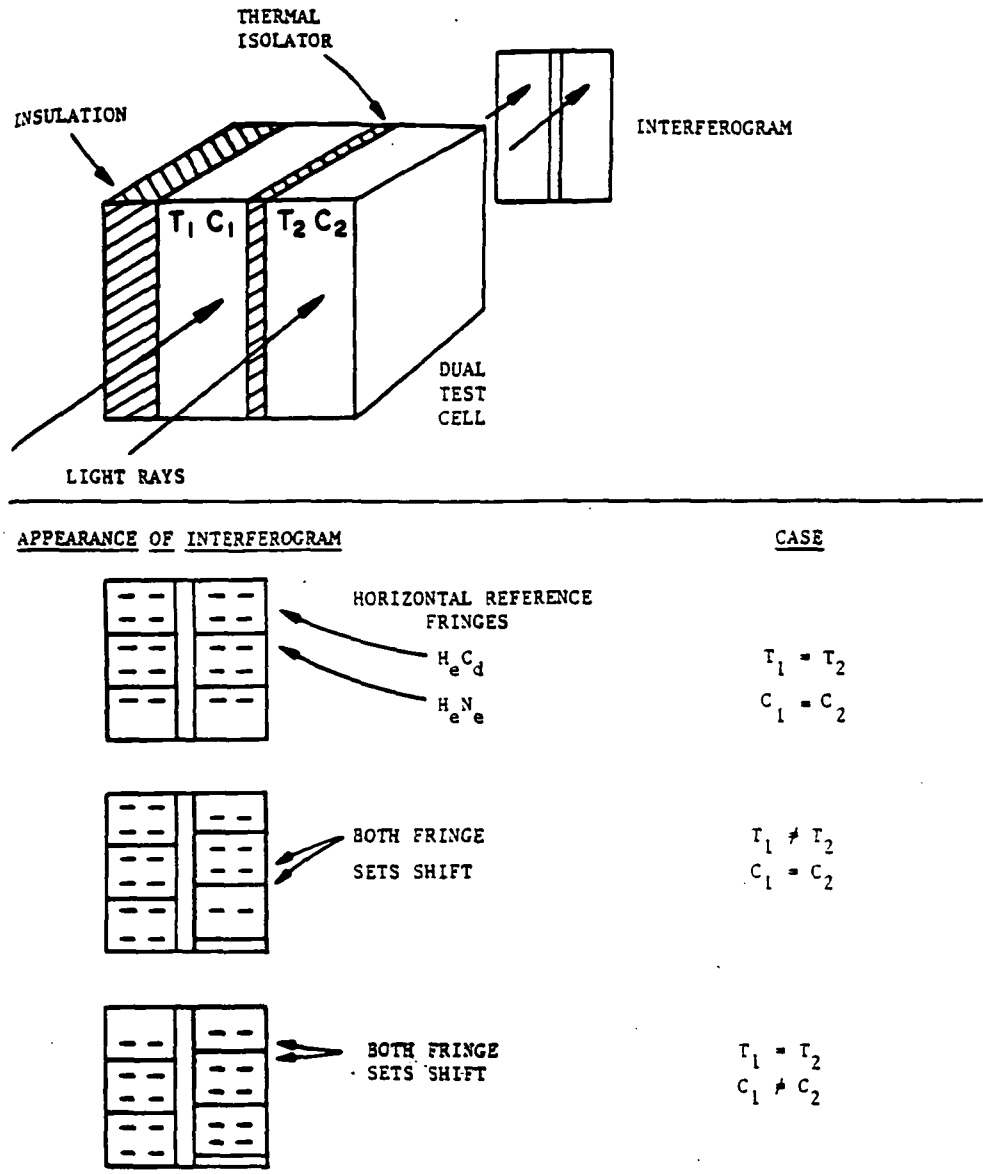

Fig. 20. How the T-CHI data should appear.

9. By sequentially examining the two differently colored interferograms at varying temperatures and concentrations in the two cells, a direct measurement of the sensitivity for separating temperature and concentration will result. In each of these cases, the required change in the temperature or concentration will be whatever is necessary to observe a phase shift in the interferogram. For conventional interferometry, this will be about one tenth of one wavelength. We anticipate about ten values of concentration and ten values of temperature difference will be required for each material.

Real Time Interferometry Case

This type of experiment will be limited for the double exposure case to temperature changes in any one step. A temperature change that causes more than one wavelength change in optical path length in one step cannot be distinguished from the value exactly an integral number of wavelengths shorter or longer. Therefore, great care must be exercised in planning the experiment for any material. A way to avoid this difficulty is to actually observe the shifting of the fringes as the temperature of concentration changes. This is possible with real time holographic interferometry. We plan to use this method for most of the data recording. The following procedure will be used for a number of materials of interest:

1. The two identical test chambers will be placed side by side in the field of view of the holocamera.

2. Known concentrations of the solution will be placed in each cell, beginning with zero concentration in both.

3. A hologram will be made at both wavelengths simultaneously.

4. The hologram will be returned precisely to its original position by using the special hologram mount made for this purpose.

5. The reconstructed wave will be superimposed on the real time wave passing through the test chamber. This will produce an infinite fringe interferogram of the test cell.

6. A tilt will be added to the object wave sufficient to produce at least two fringes in the interferogram. A 100 microradian tilt will produce finite reference fringes separated by 0.6 centimeters. This is achieved by adjusting the phase shifting element with the remote control rotary mount. The tilt will be selected so as to make the fringes run normal to the adjacent cell walls, thus crossing over both cells.

7. Then the temperature and/or the concentration in one of the cells will be increased by an amount required to increase the optical path through the cell by less than one wave. The reference fringes in the interferograms resulting from a repetition of the above steps will shift in the cell with increased temperature. This shifting will be observable in real time as the temperature is changed.

8. The interferograms are reconstructed into the 35 mm camera (first at one wavelength and then at the other) and recorded in each color. The data will take on the appearance shown in Figure 20. This provides an interferogram that can be tested for measuring temperature effects alone. It will be possible to reconstruct the two colors and observe the differences. The value of this procedure will be examined. The resulting data will be the same as that in double exposure except that many more interferograms can be taken and the real phase shifts can be observed as they develop in time.

9. The next step is to vary the concentration of the solute to examine the same effects on phase shifting or refractive index of the fluid. A similar effect on the interferogram is shown in Figure 20.

10. By sequentially examining the two different color interferograms at varying temperature and concentration differences in the two cells, a direct measurement of the sensitivity for separating temperature and concentration will result. In each of these cases, the required change in the temperature or concentration will be directly observable. For conventional interferometry, this will be about one tenth of one wavelength. We anticipate about ten values of concentration and ten values of temperature difference will be required for each material.

Since fringes can be tracked in real time, there will no ambiguity for phase shifts beyond 360 degrees.

The final test will be a demonstration of the system on a more complex temperature and concentration distribution. The cell devised for this test will have two constant temperature plates mounted horizontally in the cell. The top plate will be set at a higher temperature that the lower plate, allowing a constant temperature gradient to be established.

Multiple exposure holographic interferometry will be used as described above.

10. ANALYTICAL EXPRESSIONS TO SUPPORT THE MODELLING EFFORT TEMPERATURE CONCENTRATION, AND REFRACTIVE INDEX

Background

The theoretical evaluation of the practicality of T-CHI required representative data sets of concentration and temperature distributions that covered a wide range of materials

and experimental conditions. Generally, the solution concentration starts at values near saturation at large distances (i.e. centimeters) from the crystal face. the concentration falls off gradually nearer the face when the crystal is growing and increases near the face when the crystal is dissolving. Temperature behaves similarly, except that the variation is considerably less, with temperatures changing by less than one degree or so over the full dimension of the test chamber.

Analytical expressions were devised with parameters that allowed flexibility in testing various characteristic variations in T and C. The purpose was not to accurately describe actual T and C distributions, but to produce expressions that could be used to evaluate T-CHI models over the ranges of interest. Although the expressions were centered about actual cases encountered in a TGS crystal growth experiment (described in detail below), virtually any crystal growth case could be represented by an appropriate adjustment of the parameters in the equations. The rationale and development of the analytical expressions, as well as typical experimental values for pertinent parameters, are detailed below.

Representative T and C Distribution Expressions

A data set was produced to describe the concentration, C, and temperature, T, in a representative triglycine sulfate (TGS) crystal growth experiment. This data was to be used to calculate the refractive index field, n(r,z,t), and the resulting distribution of interference fringes. To provide the required data set, two analytical expressions were developed which approximately describe the distribution of temperature and concentration in a crystal growth experiment flown aboard Spacelab 3 in May 1985[32]. These equations, used together, allow the calculation of a time-dependent refractive index field. In addition, a third and independent equation was developed to describe directly a refractive index field in the simulated crystal growth experiment; this equation was time-dependent, yet was not a function of temperature or concentration. Although all three equations are meant to only approximately match the experimental results obtained from Spacelab 3, they are quantitative, giving specific numerical values for use in modelling.

Initial Assumptions

The geometry of a crystal growth chamber is usually very complex[33]: the TGS crystal is polyhedral and is mounted on a cylindrical thermoelectric sting which resides in a cubic enclosure. However, as a first approximation, the geometry can be greatly simplified to make it amenable to modelling by assuming spherical symmetry[33]. Furthermore, to make the equations developed here consistent with the Spacelab data in Reference 32, they are derived in cylindrical coordinates. Figure 21 presents a schematic drawing of the crystal growth chamber flown on Spacelab 1, where the spherical coordinate r and the cylindrical coordinate r and z are identified. Note that 1) the radial distance from the crystal face, r, is equal to $(r^2 + z^2)^{0.5}$, where r is the lateral distance (in cm) from

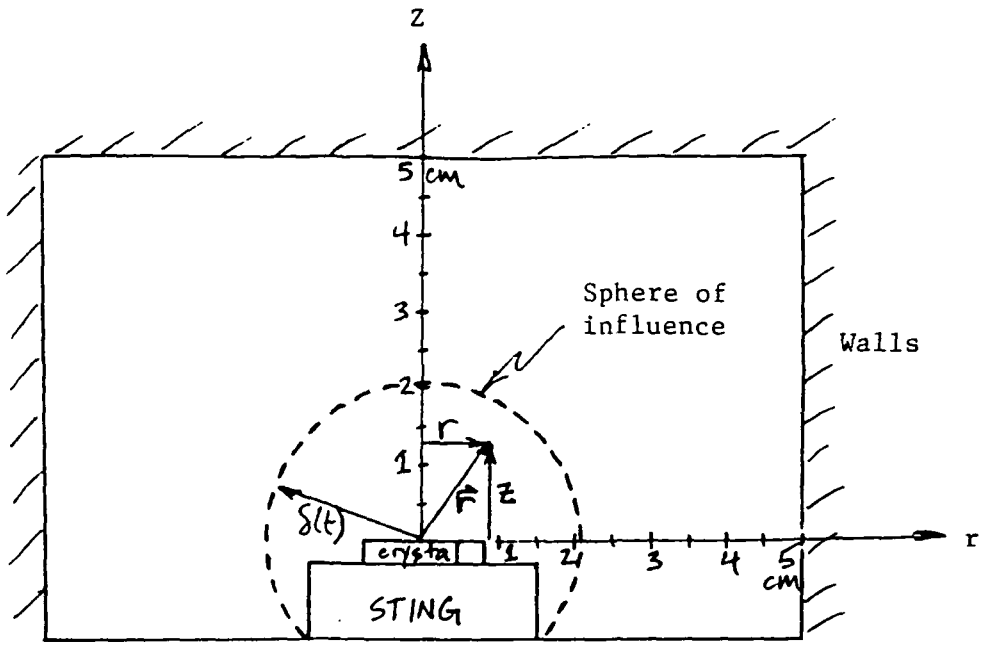

Fig. 21. Schematic drawing of crystal growth chamber with coordinates.

the cylindrical axis and z is the vertical distance (in cm) from the crystal surface, and 2) the assumption of spherical symmetry dictates that the parameters of interest are not a function of the angle about the z-axis.

Temperature

A TGS crystal growth experiment is often designed to undergo a specific temperature program. After an initial period at an elevated temperature to redissolve any recrystallized TGS, the temperature of the sting and enclosure walls usually undergoes a programmed decrease to maintain a constant rate of crystal growth. In the Spacelab 3 experiment, the temperature profile of the walls and sting consisted of three distinct phases[32].

1)	$T = 46\,^{\circ}C$	$0 \leq t \leq 0.68$ hrs
2)	$T = 46\,^{\circ}C - [(t - 0.68\text{ hrs}) \times 0.42\,^{\circ}C/hr]$	$0.68\text{ hr} \leq t \leq 9.524$ hr
3)	$T = 42\,^{\circ}C$	$9.524 \leq t$

where t is the elapsed time in hours.

Note that only the second phase was time-dependent. These expressions are not appropriate for describing the temperature of the solution: because the rate of thermal

diffusion in the TGS solution was slow compared to the rate of temperature decrease of the walls and sting, the solution at the center of the chamber was always warmer than the temperature of the perimeter during the second (cool-down) phase (see, for example, Figure 13 in Reference 32). This temperature difference was typically 0.35 °C. Note that if the relative rate of thermal diffusion was sufficiently fast, heat would be conducted from the solution to the walls and sting so quickly that temperature gradients in the solution would be negligible, and the above expressions would be acceptable for describing the solution temperature.

Although the solution temperature changed with time throughout much of the Spacelab 3 experiment, it was deemed not necessary in the current program to develop a time-dependent temperature expression for modelling purposes. Instead, the following expression for temperature, T(r,z) (in °C) (developed by close inspection of the data plotted in Reference 1), proved to be sufficiently versatile:

$$T(r,z) = T_{max} + \Delta T \left[\sin\left(\pi \frac{(r^2 + z^2)^{0.5}}{5\text{cm}} \right) - 1 \right] \qquad (21)$$

where T_{max} = maximum temperature in fluid (°C)

ΔT = difference between T_{max} and temperature of the walls and sting (a positive value in °C)

Equation 21 is valid for $(r^2 + z^2)^{0.5} \leq 5$ cm.

The first and third (isothermal) phases were trivial to model with Equation 21: ΔT was simply set to zero, and T_{max} was set to either 46 or 42 °C, respectively. The second (cool-down) phase was modelled by setting T_{max} equal to 46 °C, and by setting ΔT equal to 0.35 °C. A graph of Equation 21, showing solution temperature versus radial distance from the center of the crystal surface, is presented in Figure 22 for the second phase of temperature programming under the conditions just described.

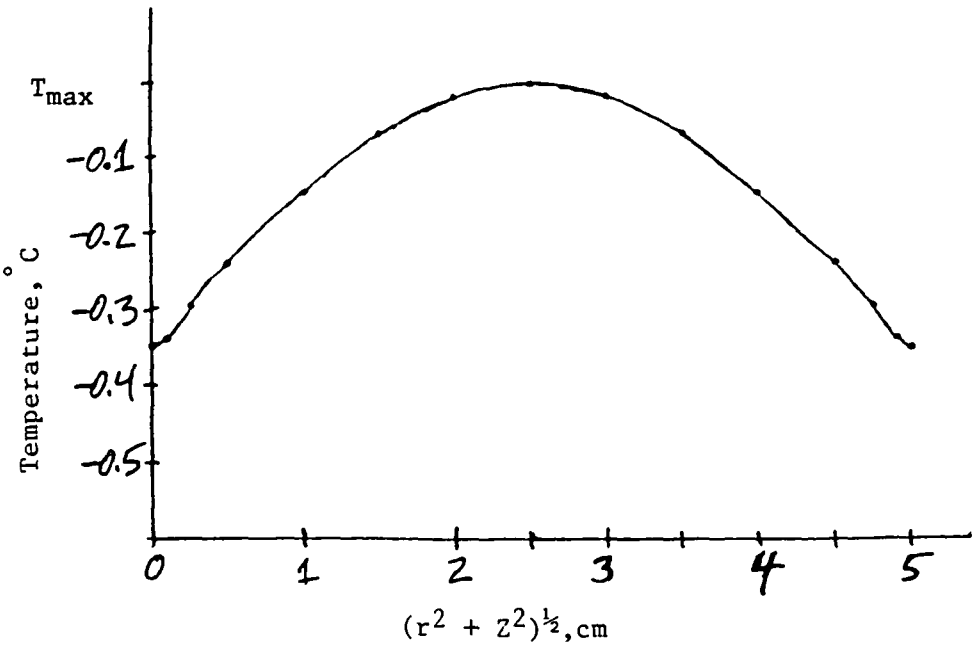

Fig. 22. Temperatures profile along any radius for $\Delta T = 0.35^{o}C$.

Concentration

The concentration profile in the Spacelab 3 crystal growth experiment was a strong function of the temperature distribution in the solution. For example, at the end of the isothermal dissolution period (0.68 hrs into the experiment), the concentration of TGS in solution was greatest at the crystal face, and decreased to the original concentration of 1.209 mmole/cm^3 at a radial distance of approximately 1 cm (see Figure 10 in Reference 32). During the linear cool-down period (phase 2 of the temperature program), there occurred a maximum in concentration at the middle of the cell, as was the case with temperature during this period (see Figure 11 in Reference 32). At the conclusion of phase 3 of the temperature program, the concentration was the reverse of that in phase 1: the TGS concentration was a minimum at the crystal face, and increased to the original concentration of 1.209 mmole/cm^3 at a radial distance of approximately 2 cm (see Figure 12 in Reference 32).

For the development of the analytical expression for concentration in the current program, it was not necessary to accurately describe the complex changes in the concentration field just described. This allowed for several simplifications to the temporal behavior of the concentration field in the Spacelab 3 experiment. First, further inspection of Figures 10 to 12 in Reference 32 revealed that the TGS

concentration never changed beyond a radial distance of approximately 3 cm: even after an elapsed time of 34 hours, "there [was] no significant change in concentration at the cap, the cell walls, or even the side of the sting"[1]. Thus, for simplicity, it was assumed that this distance, termed the "radius of influence", $\delta(t)$ (in cm), increased from zero at t = O, to 3 cm at an elapsed time of 36 hours:

$$\delta(t) = 1/2(t)^{0.5}$$

where t is the elapsed time in hours, and the scaling factor (1/2) has units of ($cm/hr^{0.5}$). This equation is simple and qualitatively matches the temporal rate at which the gradient in concentration propagates away from the crystal face in the actual Spacelab 3 experiments.

Secondly, it was assumed that a condition of constant concentration existed everywhere in the chamber at t = O, and that a monotonic drop in concentration occurred in the solution just above the crystal face as time increased. Furthermore, the concentration was assumed to increase with radial distance from the crystal until it reached the original concentration at the radius of influence. These simplifications and assumptions lead to the following analytical expression describing TGS concentration, C(r,z,t):

$$C(r,z,t) = C_{max} - 1/2\Delta C \left(\frac{t}{t_{max}}\right)\left[\cos\left(\pi \frac{(r^2 + z^2)^{0.5}}{\delta(t)}\right) + 1\right] \quad (22)$$

where t_{max} = total duration of crystal growth experiment (hours)

C_{max} = TGS concentration in far-field (can be expressed in g TGS/liter H_2O, g TGS/liter of solution, or mmole TGS/cm^3)

ΔC = change in TGS concentration from crystal surface to far-field (a positive value with same units as C_{max}).

Equation 22 is valid only for $[(r^2 + z^2)^{0.5}/\delta(t)] \leq 1$, otherwise the concentration is a constant throughout the solution (= C_{max}). Also, Equation 22 is not valid at t = 0, because $\delta(t)$ is also zero. As t goes to zero, $[(r^2 + z^2)^{0.5}/\delta(t)]$ must always be ≤ 1.

Nominal parameter values which allow Equation 22 to qualitatively match the performance of the Spacelab 3 crystal growth experiment are[32]:

t_{max} = 36 hours

C_{max} = 513 g TGS/liter of H_2O

= 391 g TGS/liter of solution

= 1.209 mmole TGS/cm^3

= 25.4 g TGS/liter of H_2O

= 19.4 g TGS/liter of solution

= 0.060 mmole TGS/cm^3

Figure 23 presents a plot of Equation 22 showing TGS concentration versus radial distance from the center of the crystal surface at t = 0,4,16, and 36 hours. As is evident in the figure, Equation 22 predicts a monotonic drop in solution concentration with radial distance from the crystal to the radius of influence, where it reaches the original unperturbed concentration.

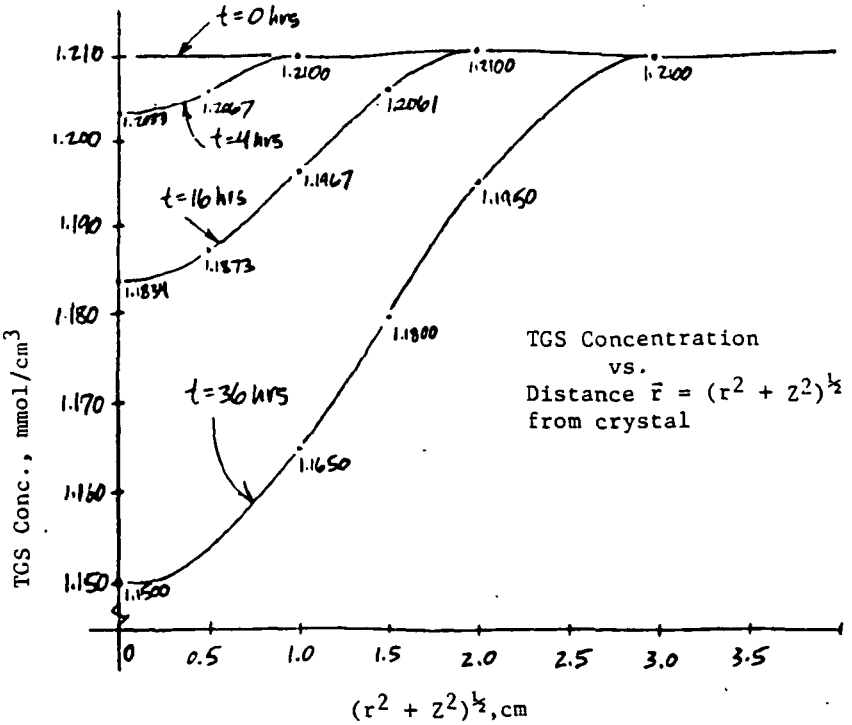

Fig. 23. TGS concentration vs. radial distance at t = 0,4,16,36 hrs.

Refractive Index

An independent equation was developed to provide a data set for the refractive index field if, for example, it was not desirable to calculate the refractive index from Equations 21 and 22. Because the variation in concentration had a much larger effect on refractive index than did the variation in temperature, the refractive index field looked much like the concentration field in Spacelab 3 experiment[32]. Therefore, the equation developed here to describe the refractive index, n(r,z,t), has the same form as Equation 22 for concentration:

$$n(r,z,t) = n_{max} - 1/2\Delta n \left(\frac{t}{t_{max}}\right)\left[\cos\left(\pi \frac{(r^2 + z^2)^{0.5}}{\delta(t)}\right) + 1\right] \quad (23)$$

where n_{max} = refractive index of solution in far-field (unaffected by crystal growth)

Δn = change in refractive index from crystal surface to far-field (a positive value).

As with Equation 22 for concentration, Equation 23 is valid only for $[(r^2 + z^2)^{0.5}/\delta(t)] \leq 1$. For $[(r^2 + z^2)^{0.5}/\delta(t)] > 1$, the refractive index is a constant throughout the solution ($= n_{max}$).

Also, Equation 22 is not valid at t = O, because $\delta(t)$ is also zero. As t goes to zero, $[(r^2 + z^2)^{0.5}/\delta(t)]$ must always be ≤ 1.

Nominal parameter values which allow Equation 23 to qualitatively match the performance of the Spacelab 3 crystal growth experiment are[32]:

t_{max} = 36 hours

n_{max} = 1.3834

Δn = 0.0006

Figure 24 presents a plot of Equation 23 showing solution refractive index versus radial distance from the center of the crystal surface at t = O,4,16, and 36 hours. As is shown in the figure, Equation 23 predicts a monotonic drop in solution refractive index just above the crystal face as time increases, and predicts an increase in refractive index with radial distance from the crystal to the radius of influence, where it reaches the original unperturbed value.

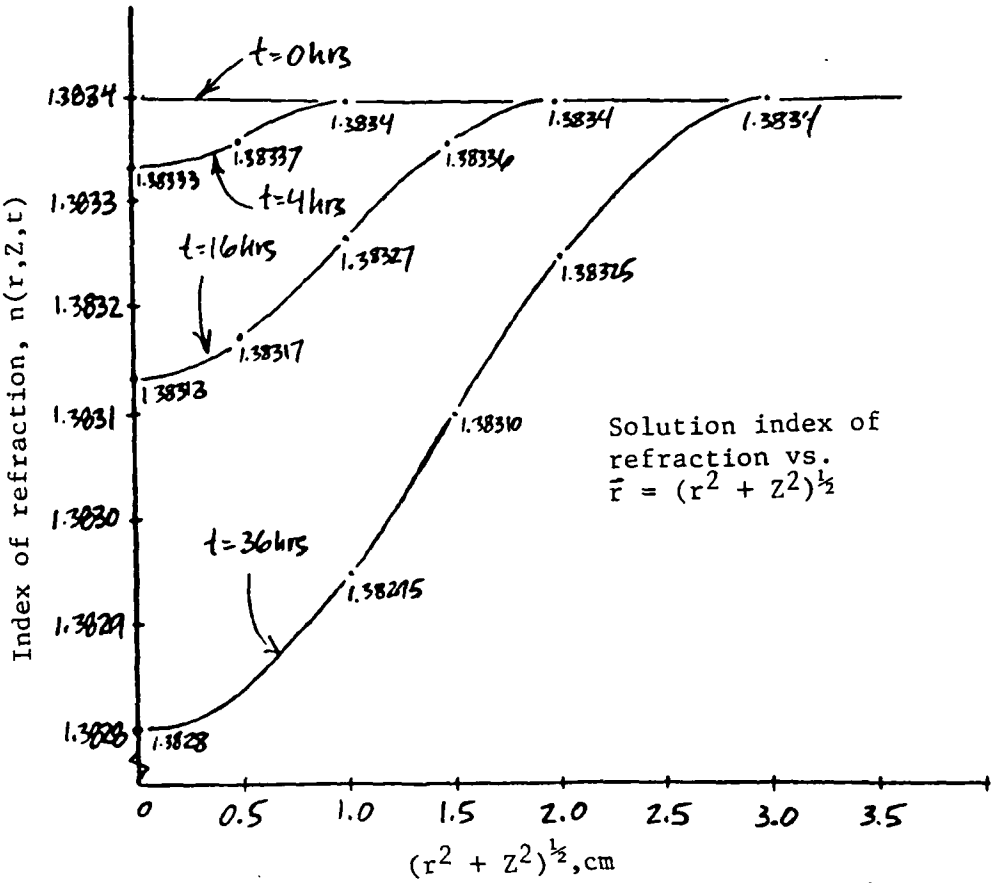

Fig. 24. Refractive Index of Solution vs. radial distance at t = 0,4,16,36 hrs.

11. CONCEPTUAL DESIGN OF A LIGHT WEIGHT, COMPACT, FIBER OPTIC-BASED HOLOGRAPHIC CAMERA SYSTEM FOR STUDIES OF CRYSTAL GROWTH IN SPACE

Background

NASA's Fluids Experiment System (FES) is an example of a space qualified crystal growth chamber which incorporates a wide range of optical diagnostic instrumentation. For example, the FES employs holography, schlieren, tomography, video imaging, and particle image displacement velocimetry. The system was designed about 10 years ago and consists of a considerable number of electro-optical components and technologies which have undergone rapid growth in the intervening years. During the past two years, the system has been expanded slightly by adding holographic optical elements (HOEs). However, a significant modification of the system, as with almost any space qualified system, would be quite complicated and expensive.

If the optical system could be redesigned using today's technology, almost every component could be replaced by a technologically superior component. The laser could be replaced with a small, light weight solid state laser; much of the large optics and lenses could be replaced with fiber optics and HOEs; and multicolor, holographic

tomography could be employed to extract concentration, temperature, and three dimensional properties. All of this could be done with a system weighing orders of magnitude less and occupying much less space than the existing FES.

If the above improvements were made on the existing FES, the modifications would most likely entail a complete rebuilding of the facility. this rebuilding, coupled with the new technologies now available allowing the miniaturization of a crystal growth chambers, will result in increased opportunities for the application of the FES. For example, a small crystal growth chamber with capabilities greater than the current FES may be incorporated into a flight deck locker, a "GAS can" experiment, or a free flyer.

Since one purpose of the breadboard is to support the design of a system ultimately intended for spaceflight, we have proposed several unique experimental options. The state of the art methods and technologies now available should be incorporated in the breadboard because their use in the space flight system is highly likely, even though they are not necessarily the best choice for evaluating the T-CHI. This can be done in such a way that their inclusion does not compromise the evaluation of the two color holographic interferometry technique, and should allow ultimate incorporation of components and geometries that favor space flight application if they prove beneficial.

We recommend that the breadboard be constructed in such a manner as to allow the evaluation of space system components. For example, photographic films will probably be used in pace because of their simplicity in recording large numbers of holograms. Other materials, like thermoplastic recording devices, cannot be ruled out entirely because they also possess important advantages. Therefore, the system should incorporate the capability for film and other recording media to evaluate cases which possess individual advantages. This part of the experiment is more supportive of the design of a space flight system than of the T-CHI technique evaluation, since the choice of film or plates should come in a design tradeoff study. For example, we already know that photographic film produces higher quality data in a laboratory environment and that film is better for space flight logistics, but a final decision must take into account the anticipated future experimental requirements and environment.

In the following sections, several conceptual designs are presented which employ state-of-the-art technology to produce the optical diagnostics segment of a generic crystal growth chamber. The conceptual designs are presented such that they can be taken either as modifications to an existing crystal growth chamber or part of a completely new chamber.

Also, the option of proceeding immediately to the construction of a spaceflight prototype, which can be used as the apparatus to conduct experimental verification and refinement of T-CHI, is discussed below.

System Design Overview

Figures 25 and 26 present schematic drawings of two versions of the proposed two color holographic system. (Note that many components described in the following overview are common to both designs.)

The sources of light are a frequency-doubled diode-pumped YAG laser (20 mW at 530 nm) and a diode laser (500 mW at 795 nm). The additional power in the small diode laser compensates for the decreased sensitivity of holographic film at a wavelength of 830 nm. The light emitted from these lasers is launched into separate optical fibers using commercial laser-to-fiber couplers. The optical fibers used throughout the system are single mode, polarization preserving fibers whose lengths are the same to within the coherence length of the lasers.

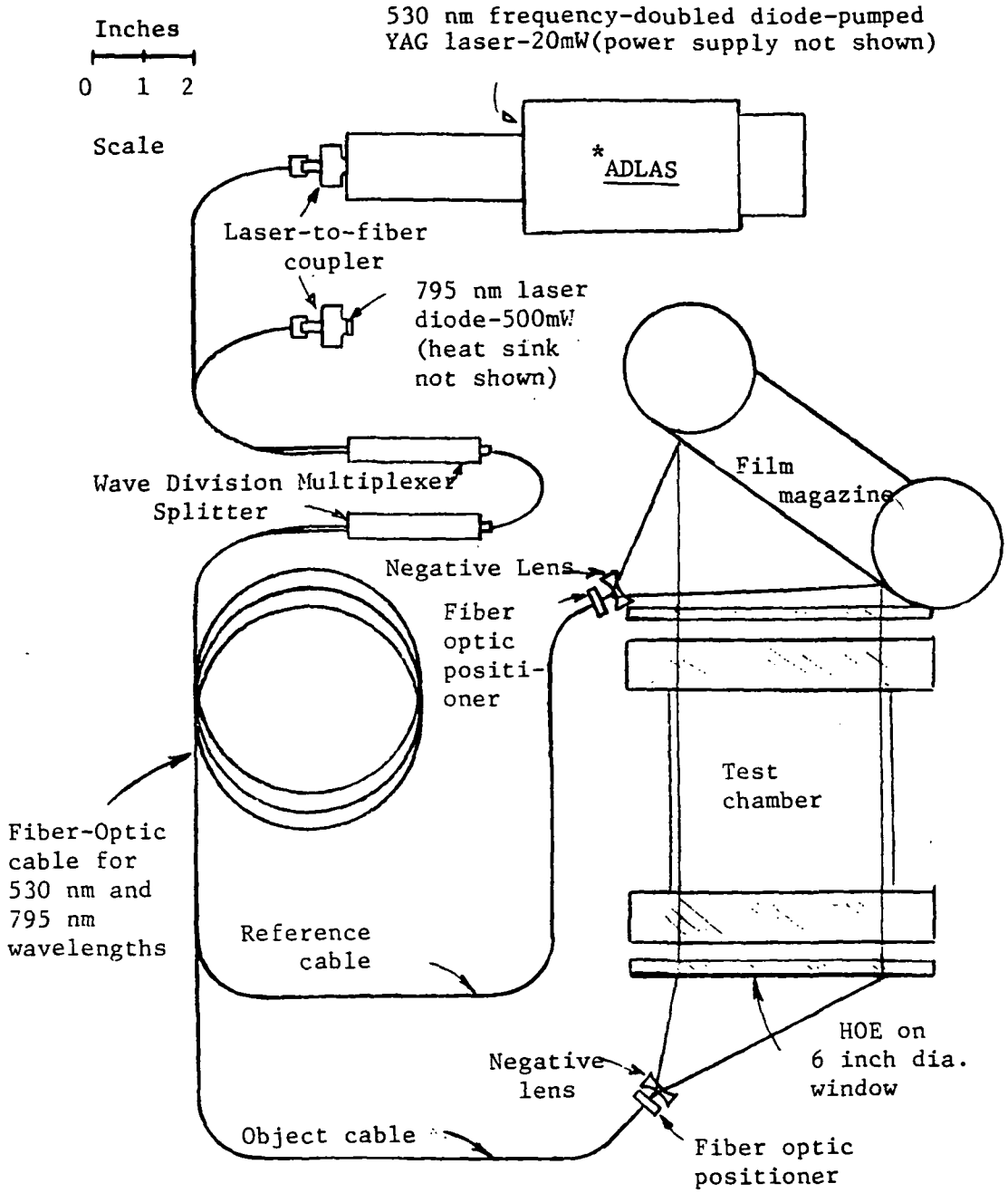

Fig. 25. Schematic drawing of a proposed T-CHI system using fiber optics and light weight compact optical components.

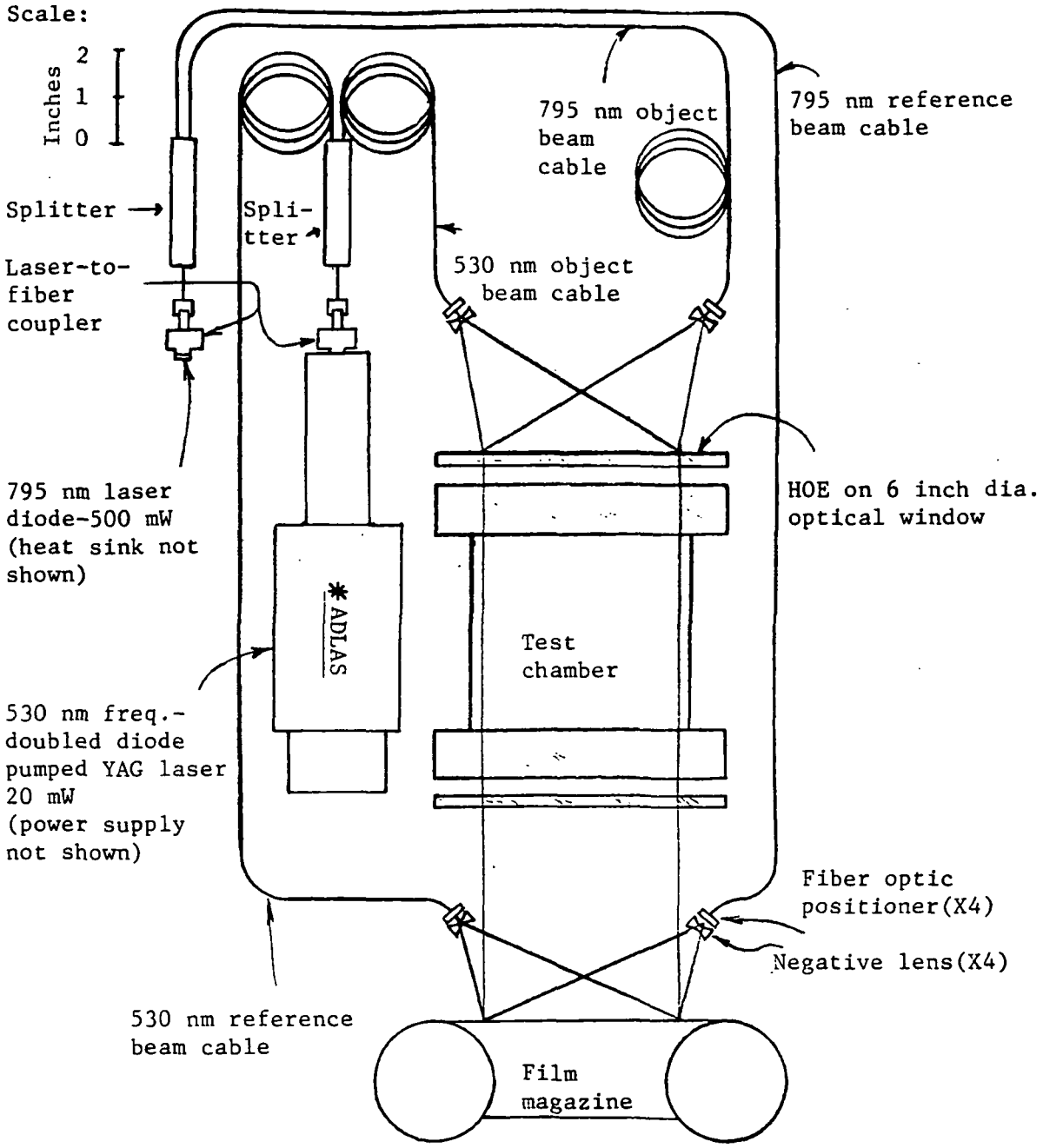

Fig. 26. Another version on the lines of the system described by Fig. 26.

In the design depicted in Figure 25, both frequencies are then mixed together and divided equally into two fibers by one of two methods:

1) The two frequencies are mixed in a **wave division multiplexer**, and propagated through a single fiber to a **splitter** (this is the method shown in Figure 25). The splitter distributes half of the energy at each wavelength into two separate fibers, with the result that each fiber propagates approximately 10 mW of 530 nm light and 50 mW of 830 nm light (the actual power in each fiber is somewhat less due to various losses occurring during launching, division, and mixing).

2) Both frequencies are coupled at the input of a **variable directional coupler** and distributed internally into two output fibers. By changing the core-to-core distance within the coupler, the optical power can be continuously varied between the two output fibers.

An alternative to mixing the two frequencies is depicted in Figure 26. In this design, each fiber is connected to a splitter immediately after the beam is launched. The splitters divide each beam into two fibers, giving a total of four output fibers. Two of these output fibers, each containing a different wavelength, can then be positioned before the test cell to act as the object beams, while the other two are positioned after the test cell and act as reference beams.

The optical fiber (or fibers, depending on the specific design) containing the object beams is directed to one or two (again, the number depends on the specific design) short focus negative lenses positioned in front of the test cell. This lens (or lenses) expands the two object beams onto HOE affixed to the 0.25 inch thick, 6 inch diameter optical glass window of the test chamber. The HOE is a 20 micron thick layer of gelatin with negligible weight, designed and constructed to collimate the steeply diverging laser beams. It therefore replaces a conventional 150 mm diameter glass lens of approximately unity f/number. The collimated beams, with a diameter of approximately 4 inches, are directed through the crystal growth test chamber to a film magazine for holographic recording.

The other optical fiber (or fibers), containing the reference beams, is positioned at a second negative lens (or lenses) located after the test chamber. This lens (or lenses) expands the two reference beams onto the film magazine, where they interact with the object beams to create the holographic image on the film surface.

Component Specification

Table 4 presents vendor information, including model numbers and approximate dimensions, weights, and prices for the individual components in Figure 25. The list of vendors and model numbers is not exhaustive; it is meant to illustrate representative

TABLE 4. VENDOR, MODEL NO., AND APPROXIMATE DIMENSIONS, WEIGHT, AND COST

ITEM	VENDOR AND MODEL NO.	DIMENSIONS (inches)	WEIGHT	COST
Frequency-doubled dode-pumped YAG laser (20mW at 530um)	Adlas/AB Lasers; Model 215C	Laser Head: 9.1 x 2.8 x 2.2 Power supply: 4.8 x 4.1 x 2.4	Total: 4.65lbs	$15,900
Diode Laser (500mW at 795nm)	Spectra Diode Labs: Model SDL-2432-H1	1.5 x 1 x 1 max	1 lb max	$ 3,300
Laser-to-fiber coupler coupler (2 required)	OZ Optics Ltd.; Model HULD-1	1 x 0.8 dia.	<0.2 lbs ea.	$ 1,000 (2 x $500)
Wave Division Multiplexer and Splitter	JDS Ltd.; custom item	3 x 3 x 3 max	1 lb max	$ 1,200 to 3,000
Optical Fiber (2 pieces required for design in Figure 1)	Alcoa Fujikura Ltd; 830nm:Model SM85-P 530nm:Model SM48-P	0.125 dia x 36 long	<0.2 lbs ea	$ 40 (2 x $20)
Negative lens and mount (2 sets required for design in Figure 1)	Melles Griot; 01 LLD series lens, 07 LHF 009 mount w/07 LAD series adaptor	0.5 x 2 dia	<0.2 lbs ea	$ 180 (2 x $90)
Holographic Optical Element	Optical Images, custom items	20 microns x 6 dia	negligible	$ 3,000

products which show promise in filling the requirements of a two color holographic system.

Advantages

The overall advantages to the above designs are a reduction in weight, volume, and complexity. For example, use of optical fibers requires less optical hardware because beam steering is simplified, eliminating the need for bulky mirrors, beam splitters, and mounts. The HOE, being only 20 microns thick, weighs less than 3/100 ounce, yet takes the place of a fast 6 inch diameter lens and mount weighing on the order of 5 pounds. The diode laser easily fits within the palm of a hand, yet has a power output 4 times greater than the HeNe laser currently flown in the FES.

Another advantage is increased flexibility. The fiber optics allow for the placement of individual system components in a variety of configurations without extensive modifications to the instrument. For example, the object beams are shown for convenience in Figure 26 on opposite sides of the test cell centerline (as are the reference beams), yet in actuality they could be placed side-by-side if that configuration proved advantageous, or they could be placed at any intermediate position, without extensive modifications.

A fiber optic based system can be made much more rugged than a system which must use large mirrors and beam splitters. Mirrors and beam splitters are highly vulnerable to misalignment during launch. Fiber optical systems employing the designs shown here are extremely rugged and would retain alignment under the most adverse conditions.

Cleanliness is another factor which is improved significantly by use of fiber optics. Mirrors and beam splitters which are exposed to the environment almost always attract dust, scratches, and contaminants that ultimately reduce the quality of data. Fiber optics provides a simple way to maintain a clean light beam for both the object and reference beams.

Because fiber optics and holographic optical elements allow for miniaturizing the optical system, additional view angles and diagnostic equipment can be added to a crystal growth cell.

Technical Considerations and Challenges

As described above, the second phase of the present study requires the construction of a two color holographic interferometry system to carry out the experimental verification and refinement of T-CHI and to make some of the required measurements of material properties. We initially provided a design for a conventional optical system employing standard commercial components. The question which immediately comes to mind is "Why not construct a fiber optic/laser diode system such as one designed above to serve that purpose?" The system cost appears to be similar, and the system capability would

appear to be greater. However, a number of critical issues do exist in the new state-of-the-art designs. Some risks are involved if a fiber optic system is to be used both as a laboratory instrument as well as a precursor to a space system. These tradeoffs are described here. The final decision must consider the tradeoffs and risks, and the ultimate goals of the program.

There are three important factors driving the choice of lasers in the development of a two color holographic instrument. First, the lowest operating wavelength currently available in a solid-state laser is 530 nm. Second, it is advantageous to have the two wavelengths as different as possible to maximize the sensitivity of the technique. third, the sensitivity of all commercially available holographic films degrades rapidly at infrared wavelengths. for example, using Kodak 120-02 film, a 150 times greater energy density is required to achieve an equivalent exposure at a wavelength of 787 nm compared to 633 nm (the primary HeNe laser wavelength)[34]. The first and second factors suggest that a 530 nm laser is a good candidate for the shorter wavelength laser, and, in fact, a commercially available model exists with excellent specifications (see Table 4). The second and third factors dictate that a balance must be reached in the choice of the longer wavelength laser: its wavelength should reside as far as possible in the infrared without the wavelength becoming so long as to require an enormous amount of power to achieve an adequate exposure. The diode laser specified in the current design attempts to provide such a balance: it has an operating wavelength of 795 nm and a specified output power of 500 mW. assuming a launching efficiency of approximately 70% (see the discussion in the next two paragraphs), this allows an exposure with an optical density of 0.8 (considered optimum with commercially available holographic films[35]) to be achieved in approximately 0.4 seconds using 10E75 film[34].

Optical fibers are manufactured to maximize the transmission of a specific wavelength. However, the present application requires only a few meters of fiber, so beam attenuation is not a concern even if the wavelengths differ somewhat from the optimal wavelength for the particular fiber being used. Of much greater concern is the reduction of beam intensity in the fiber coupler. When coupling light into a monomode fiber, it is advantageous to use a high precision fiber coupler with x-, y-, and z-adjustments for the fiber end face, as well as fine tilt adjustment[36]. Launching efficiencies of 60 to 70% are then obtainable with beams of circular cross section.

Many solid-state lasers, including the 795 nm diode laser specified here, emit a diverging beam with an elliptical cross section. This requires either special optics to focus the beam to a circular cross section to optimize launching efficiency, or the beam can be launched with no correction with reduced efficiency. In the absence of correction, the focussed elliptical beam has a different waist diameter along each axis of the ellipse. The coupler is then chosen so that the focussed waist diameter of the minor axis is approximately the same as the fiber core, which has a circular cross section. Thus, the fiber acts as a spatial filter as the elliptical beam is launched by the coupler, and the launching efficiency is reduced because the laser light at the wings of the major axis is not launched. One advantage to this method is that the beam

emerging from the fiber has a circular cross section needing no further correction. a diode laser-to-fiber coupler is available commercially which achieves a launching efficiency of 35% with no elliptical-to circular correction[37]. Additional research is necessary to determine the most effective approach to ensure adequate launching efficiency while ensuring adequate beam quality.

The wave division multiplexer, splitter, and variable directional coupler, used here either singly or in combination to mix the two wavelengths into the same fiber, are usually performance optimized for one wavelength. Additional research is necessary to determine the best design of the individual components, to minimize power losses during the mixing process.

Additional power is lost in the HOE which, acting as a diffraction grating, distributes the laser light into many orders, of which the first order is the only one used. thus, the overall efficiency of the system in delivering light to the test section is an area of concern which will be addressed in detail during system development.

12. CONCLUSIONS

The work was the first critical evaluation of the T-CHI technique dealing with crystal growth experiments. the general theory of the technique has been developed along with extensive numerical discussions using TGS aqueous solution as an example. The analytical expressions developed can be used for any prospective system. Teledyne Brown Engineering's SOQ code has also been successfully utilized for predicting interferometric fringes and inverse determination of the temperature and concentration variations. One basic finding is that small temperature and concentration changes yield significant changes in the fringe orders. Thus, even if single color interferometry is used, one of the quantities must be already known very precisely. T-CHI technique thus provides the natural choice as well as new challenges. As stated in the report, these challenges can be successfully handled by us in the option part of the contract. Our breadboard design is based on these opportunities. Ultimately intending spacecraft applications, we have proposed several unique experimental options. These future developments will open a unique door in understanding the crystal growth phenomena here on earth as well as in space.

References

1. R. B. Owen, J. Opt. Soc. Am. 71, 1566 (1981).

2. R. B. Owen, Appl. Opt. 21, 1349 (1982).

3. R. B. Owen, J. Opt. Soc. Am. 72, 1762 (1982).

4. R. B. Owen, C. Riley, H. D. Coble and V. S. Alter, J. Opt. Soc. Am. 73, 1947 (1983).

5. M. H. Johnston and R. B. Owen, Met. Transac. A, 14A, 2163 (1983).

6. M. H. Johnston, R. B. Owen and R. E. Shurney, NASA Technical Paper 2110 (1983).

7. R. B. Owen and M. H. Johnston, Opt. Lasers. Eng. 5, 95 (1984).

8. R. J. Collier, C. B. Burckhardt and L. H. Lin, Optical Holography (Academic, New York, 1971).

9. H. J. Caulfield, Handbook of Optical Holography (Academic, New York, 1979).

10. C. M. Vest, Holographic Interferometry (John Wiley & Sons, New York, 1979).

11. P. Hariharan, Optical Holography: Theory, Techniques and Applications (Cambridge University Press, Cambridge, 1984).

12. J. F. Flannery and R. F. Wuerker, J. Opt. Soc. Am. 71, 1567 (1981).

13. R. B. Owen, M. H. Johnston and R. B. Lal, J. Opt. Soc. Am. A1, 1221 (1984).

14. R. B. Owen and R. L. Kroes, Optics News 11(7), 12 (1985).

15. R. B. Owen, R. L. Kroes and W. K. Witherow, Opt. Lett. 11, 407 (1986).

16. B. P. Hildebrand and J. D. Trolinger, Appl. Opt. 22, 2124 (1983).

17. W. K. Witherow, Appl. Opt. 26, 2465 (1987).

18. H. D. Yoo, W. R. Wilcox, R. Lal and J. D. Trolinger, J. Crystal Growth 92, 101 (1988).

19. J. D. Trolinger, Proc. SPIE 816, 128 (1988).

20. P. A. Ross, Application of a Two-Wavelength Interferometr to the Study of a Simulated Drop of Fuel, Ph.D. Thesis, University of Wisconsin (1960).

21. M. M. El-Wakil and P. A. Ross, A Two Wavelength Interfermetric Technique for the Study of Vaporization and Combustion of Fuels, Liquid Rockets and Propellanta, in Progress in Astronautics and Rocketry, Vol. II, Academic Press New York (1960).

22. F. Mayinger and W. Panknin, Holography in Heat and Mass Transfer, Proceedings of the 5th Int. Heat Transfer Confr., Tokio (1974).

23. F. Mayinger and W. Panknin, in Combustion Measurements, R. Goulard (ed.), Academic, New York (1976) pp. 270-283. See also references cited therein.

24. A. Ecker, G. J. Schmitz and P. R. Sham, in Proceedings of the Norderney Symposium on SCIENTIFIC RESULTS OF THE GERMAN SPACELAB MISSION D1, Norderney, Germany, 27-29 August, 1986, pp. 212-216.

25. A. Ecker, Solidification Front Dynamics Examined by Holographic Interferometric Measurement of Temperature and Concentration Using Transparent Model Systems, Final Report, NASA, March 1987. See also references cited therein.

26. A. Ecker, Two Wavelenth Holographic Measurement of Temperature and Concentration During Alloy Solidification, AIAA, 25th Aerospace Sciences Meeting, Reno, Nevada, January 12-15, 1987; J. Thermophys Heat Transfer 2, 193 (1988).

27. A. Ecker, J. Iwan, D. Alexander and D. O. Frazier, Fluid Flow in the Melt of Solidifying Monotectic Alloys, Proc. 6th European Symp. on Material Sciences Under Microgravity Conditions, Bordeaux, February, 1987.

28. J. D. Trolinger, Opt. Eng. 19, 722 (1980).

29. Reference 10, Chapter 6.

30. R. L. Kroes and D. Reiss, J. Crystal Growth 69, 414 (1984).

31. C. G. Murphy and S. S. Alpert, Am. J. Phys. 39, 834 (1976).

32. H. D. Yoo, W. R. Wilcox, R. Lal and J. D. Trolinger, J. Crys. Growth 92, 101 (1988).

33. L. C. Liu, W. R. Wilcox, R. Kroes and R. Lal, in Materials Processing in the Reduced Gravity Environment of Space, Ed., G. Rindone North-Holland, Amsterdam, 1982, p. 389.

34. J. A. Davis and M. F. Brownell, Opt. Lett. 11, 196 (1986).

35. J. D. Trolinger, Laser Applications in Flow Diagnostics, AGARDograph No. 296, NATO 1988, p. 63.

36. H. I. Bjelkhagen, Opt. Eng. 24, 645 (1985).

37. Sezerman, Oz Optics Ltd., Carp, Ontario, Canada, private communication, 29 January, 1990.

Report Documentation Page

1. Report No.	2. Government Accession No.	3. Recipient's Catalog No.
4(Final)		

4. Title and Subtitle

TWO COLOR HOLOGRAPHY CONCEPT(T-CHI)

5. Report Date

3-20-90

6. Performing Organization Code

7. Author(s)

C.S.Vikram,H.J.Caulfield,G.L.Workman,J.D.Trolinger, C.P.Wood,R.L.Clark,A.D.Kathman and R.M.Ruggiero

8. Performing Organization Report No.

4(Final)

10. Work Unit No.

9. Performing Organization Name and Address

Center for Applied Optics
The University of Alabama in Huntsville
Huntsville,Alabama-35812

11. Contract or Grant No.

NAS8-38078

13. Type of Report and Period Covered

FINAL
5-11-89 to 3-11-90

12. Sponsoring Agency Name and Address

NASA George C. Marshall Space Flight Center
Marshall Space Flight Center,Alabama-35812

14. Sponsoring Agency Code

15. Supplementary Notes

16. Abstract

This is the final report of the Two-Color Holographic Interferometry(T-CHI) project. For the first time,the technique is critically investigated in the study. The study is in connection to temperature and concentration determination in crystal growth experiments.General analytical methodology is developed with specific examples for triglycine sulphate (TGS) crystal growth situation.Theory for determining temperature and concentration from holographic fringes,sensitivity,accuracy,etc. are described in detail.Modeling and error analysis is performed using simple cell model as well as a practical onion-like distribution.Simple cell model is described analytically whereas the onion-like distribution is handled by Teledyne Brown Engineering's System Optical Quality(SOQ) code.Finally,a few designs of the experimental approach"breadboard" are described in detail.These designs will ultimately help confirming experimentally what has been shown in this report and in further space-flight applications.The entire study keeps in mind the contemporary problems as well as state of the art to solve them.

17. Key Words (Suggested by Author(s))

Holography,two-colors,crystal growth, temperature,concentration,space applications,TGS,modeling,breadboard design

18. Distribution Statement

19. Security Classif. (of this report)	20. Security Classif. (of this page)	21. No. of pages	22. Price
Unclassified	Unclassified	65	

NASA FORM 1626 OCT 86